TU Delft

Delft University of Technology

CFD modeling approach for late-injection methanol sprays validated with ECN spray M

Zoumpourlos, Konstantinos; Bekdemir, Cemil; Geertsma, Rinze; van de Ketterij, Robert; Coraddu, Andrea

DOI
10.1177/14680874251323931

Publication date
2025

Document Version
Final published version

Published in
International Journal of Engine Research

Citation (APA)
Zoumpourlos, K., Bekdemir, C., Geertsma, R., van de Ketterij, R., & Coraddu, A. (2025). CFD modeling approach for late-injection methanol sprays validated with ECN spray M. *International Journal of Engine Research*, *26*(8), 1202-1223. https://doi.org/10.1177/14680874251323931

Important note
To cite this publication, please use the final published version (if applicable).
Please check the document version above.

Copyright
Other than for strictly personal use, it is not permitted to download, forward or distribute the text or part of it, without the consent of the author(s) and/or copyright holder(s), unless the work is under an open content license such as Creative Commons.

Takedown policy
Please contact us and provide details if you believe this document breaches copyrights.
We will remove access to the work immediately and investigate your claim.

This work is downloaded from Delft University of Technology.
For technical reasons the number of authors shown on this cover page is limited to a maximum of 10.

Green Open Access added to TU Delft Institutional Repository
as part of the Taverne amendment.

More information about this copyright law amendment
can be found at https://www.openaccess.nl.

Otherwise as indicated in the copyright section:
the publisher is the copyright holder of this work and the
author uses the Dutch legislation to make this work public.

Check for updates

International Journal of ENGINE RESEARCH

Original Research Article

International J of Engine Research
2025, Vol. 26(8) 1202–1223
© IMechE 2025
Article reuse guidelines:
sagepub.com/journals-permissions
DOI: 10.1177/14680874251323931
journals.sagepub.com/home/jer
Sage

CFD modeling approach for late-injection methanol sprays validated with ECN spray M

Konstantinos Zoumpourlos[1], Cemil Bekdemir[3], Rinze Geertsma[1,2], Robert van de Ketterij[2] and Andrea Coraddu[1]

Abstract

To reduce emissions, methanol is a favorable carbon-neutrally-producible alternative fuel, which can substitute gasoline in direct-injection spark-ignition (DISI) engines. Robust DISI engine operation relies on a consistent air-fuel mixture. To understand the physical processes that characterize the mixture formation, predictive computational fluid dynamics (CFD) simulations are used to improve the understanding, operation, and emissions of these engines. However, using an alternative fuel such as methanol often poses challenges to the CFD simulations' validity due to the alteration of the fuel properties. This study presents the validation of a CFD modeling approach that can be applied to the predictive modeling of DISI methanol engines. Our methodology uses Lagrangian-Eulerian methods to model the methanol eight-hole counter-bore style Spray M injector from the Engine Combustion Network (ECN). We used the Spray M1 condition, which represents a late-injection spray under a high ambient pressure and temperature environment. For the present study, we employed both a Reynolds Averaged Navier Stokes (RANS) and a Large Eddy Simulation (LES) turbulence approach in CONVERGE-CFD. To validate our models, we used the projected liquid volume (PLV) maps generated by the tomographic liquid volume fraction (LVF) based on methanol. Subsequently, we tuned our models based on the corresponding numerical predictions of the liquid penetration and LVF distributions. The results demonstrated that both the RANS and LES models could replicate the spray morphology and liquid length. While the RANS model was unable to fully capture the complex phenomena of spray collapse and sweeping in the methanol multi-hole spray, the LES model effectively reproduced these behaviors without excessive tuning effort.

Keywords

Computational fluid dynamics, engine combustion network, Spray M, methanol, alternative fuels, late-injection

Date received: 4 October 2024; accepted: 20 December 2024

Introduction

In the transportation sector, spark ignition (SI) internal combustion engines (ICEs) are mainly used in light and medium-duty vehicles inducing CO_2, and other harmful emissions such as NO_x, unburned hydrocarbons (UHC), CO, and soot.[1–3] Despite the recent progress of electrified vehicles, ICEs persist as the main powering solution due to their high energy density, range, and reduced cost.[4,5] Moreover, the increased deployment of direct-injection spark-ignition (DISI) engines over the outdated port fuel injection (PFI) technology improved the efficiency and emissions of SI engines.[6,7] To further reduce exhaust emissions and achieve the desired climate targets, alternative fuels produced from carbon-neutral sources can decarbonize ICEs.[8,9] Methanol is regarded as a promising alternative fuel, capable of substituting gasoline in DISI engines,[10] or used as a premixed fuel in dual-fuel compression ignition engines in the marine sector.[8] In particular, methanol possesses favorable combustion properties, such as high burning velocity, low combustion temperature and high octane number resulting in reduced NOx and soot emissions compared to gasoline.[2,11,12] Methanol remains in liquid

[1]Delft University of Technology, Delft, The Netherlands
[2]Netherlands Defence Academy, Den Helder, North Holland, The Netherlands
[3]TNO Powertrains, Helmond, The Netherlands

Corresponding author:
Konstantinos Zoumpourlos, Faculty of Mechanical Engineering, Department of Maritime and Transport Technology, Delft University of Technology, Mekelweg 2, Delft 2628 CD, The Netherlands.
Email: k.zoumpourlos@tudelft.nl

form under atmospheric conditions, making storage and handling similar to those of conventional fuels.[11] Its production can be scaled up, and it effectively offers a higher energy density than other alternative fuels such as ammonia and hydrogen.[13,14] Given these considerations, methanol is considered a viable option for direct injection (DI) engines.

With respect to both efficient combustion and low emissions, the performance of DI engines depends on the formation of a homogeneous mixture through the spray and evaporation phenomena.[7] Therefore, studying the spray formation is fundamental for the control, performance, and emissions of DI engines. Computational fluid dynamics (CFD) can be employed to analyze and predict in-cylinder engine phenomena, such as spray development, mixture formation, and combustion.[15]

Using CFD to investigate methanol spray and combustion can be challenging due to the lack of dedicated methanol experimental data. Existing CFD modeling practices have only been verified using conventional fuels, which are calibrated based on their physical properties. Contrary to that, the physical properties of methanol differ largely from gasoline. Methanol's latent heat of vaporization is approximately four times higher than gasoline's, which enhances the evaporation cooling effect observed in DI engines.[11] Furthermore, at elevated injection temperatures, methanol has an augmented vapor pressure and a lower boiling point. This makes it more volatile than gasoline and increases in-nozzle cavitation phenomena. This inherent disparity between the properties of methanol and gasoline impacts the spray structure and evaporation phenomena, and thus, the lack of methanol experimental data renders the validity of CFD simulations questionable.

Previous experimental research revealed that under low ambient temperatures, methanol displays a different spray structure compared to gasoline.[16–19] These conditions comprised of low to medium injection pressures (50 to 150 bar), and variable ambient environments ranging from atmospheric to sub-atmospheric conditions linked to cold-start operation.[17,18] While methanol demonstrated a similar spray structure with gasoline under barely evaporating conditions,[16] its higher volatility increased the evaporation rate and spray cone angle.[18] In another study by Zeng et al.[17] in a sub-atmospheric pressure environment, increasing the methanol temperature caused a faster transition to flash-boiling spray which can potentially enhance the cold-start performance.

Recent experimental studies have employed more engine-relevant multi-hole counter-bore gasoline injectors using methanol and iso-octane in increased ambient temperature environments. Particularly, the study of Badawy et al.[20] revealed a more pronounced difference in the methanol spray structure under realistic DISI conditions. In the same study, even at atmospheric pressure and 80°C fuel temperature, the methanol spray plumes displayed evident spray collapsing. highlighting a significantly different structure than iso-octane. Furthermore, the engine combustion network (ECN)[21] has conducted methanol spray experiments using an eight-hole counter-bore injector under the same conditions as Spray G[22]. These new Spray M experiments[23] consist of a late-injection, stratified DISI operation dataset, and an early-injection flash-boiling condition dataset. Similarly, with the findings of Badawy et al.,[20] the ECN results showed strong spray collapsing phenomena for both tested conditions, confirming the influence of methanol's volatility. In addition, using a set of ECN Spray G conditions, Hwang et al.[24] compared iso-octane with di-isobutylene surrogate, olefinic, and the 30% ethanol blend (E30) sprays. Under the tested conditions, the non iso-octane fuels demonstrated plume collapsing due to higher volatility. These findings strongly indicate that the vapor pressure influences the spray structure under DISI engine operation.

Concerning methanol engine studies, the focus was mainly on investigating combustion performance and emissions.[25–28] Due to methanol's high latent heat of vaporization, a strong cooling effect is introduced during the mixture formation, which lowers the in-cylinder temperature, and may cause cyclic variability and wall impingement.[14] Wouters et al.[29] demonstrated that methanol wall film formation is three times stronger than in gasoline operation, due to the slower evaporation rate. Matamis et al.[28] conducted experiments in an optically accessible heavy-duty methanol engine and showed increased ignition delay. This cooling-effect-induced ignition delay impeded the flame propagation, demonstrating the effect of methanol sprays during engine operation. Furthermore, Dierickx et al.[30] observed that the intensified cooling effect resulted in methanol condensation within the intake manifold. As a result of the reported lower in-cylinder and intake air temperatures, NO_x emissions and heat losses decreased compared to diesel[25–27,30] and gasoline operation.[29] Thus, methanol operation diminishes the trade-off between thermal efficiency and emissions while improving the carbon footprint.[31]

With respect to CFD modeling studies, very limited research has been conducted on methanol sprays in DI conditions due to experimental data scarcity. The recent Spray M experiment is the first publicly available dataset, which provides a validation basis for future methanol-dedicated spray modeling approaches.[23] Furthermore, Duronio et al.[32] applied a novel unified droplet breakup modeling approach to simulate the Spray G and M conditions. To eliminate the tuning effort of state-of-the-art breakup models, their approach combined a flash-boiling effervescent model with a dynamic aerodynamic breakup model and successfully recreated the methanol and E00 experiments in both late and early-injection conditions. Before the recent methanol ECN datasets, previous computational efforts mainly used the established Spray G[22] datasets to tune and validate Lagrangian spray models

employing iso-octane[33–36] and E30.[37] Using a similar approach, Moreno Cabezas et al.[38] validated their volume-of-fluid (VoF) and Lagrangian modeling framework based on the iso-octane ECN Spray G. Following this, they converted the model for methanol injection using the same injection and ambient conditions. Their results illustrated increased spray plume angles for the methanol injection, confirming past experimental observations.[18] However, with the recent understanding from Spray M, the CFD model was expected to predict plume collapsing due to the volatility of methanol.

This suggests that the conventional state-of-the-art modeling approaches are not sufficient for predicting the methanol vapor pressure and latent heat effects on spray formation. While the use of iso-octane datasets and modeling frameworks offers a solid foundation for understanding DISI sprays, it is imperative to transfer this knowledge to alternative fuels like methanol. Thus, to ensure robust tuning and calibration of CFD models, methanol-dedicated experimental data should be employed.

Aim & novelty

This paper aims to model the ECN methanol Spray M experiment using the Lagrangian-Eulerian framework. The novelty of the present study comprises the presented modeling framework, which is able to capture the complex multiphase flow phenomena of methanol injection. While previous studies have demonstrated that CFD modeling can accurately replicate the ECN spray G data using iso-octane, such a CFD study using the recent methanol Spray M data for the tuning of the conventional wave breakup model is missing. Therefore, to accurately model sprays and understand the impact of methanol in the mixture formation, CFD model calibration should be conducted using proper methanol experiments.

For our analysis, we applied a spray model using CONVERGE-CFD[39] applying both Reynolds Averaged Navier Stokes (RANS) and Large Eddy Simulation (LES) turbulence modeling. Using both turbulence approaches, we tested the ability of each model to capture the plume-collapsing behavior of methanol under the designated DISI conditions. Our aim was to adequately predict the experimental trends using the computationally cheap RANS models, which can be employed for full engine CFD simulations at a later stage. Accordingly, the RANS models were compared with the more high-fidelity computationally-intensive LES approach.

For model validation, we used the spray M1 experimental condition, which corresponds to late-injection stratified DISI conditions. These conditions are characterized by an increased ambient pressure and temperature. To compare our numerical results with the experiments, we used the projected liquid volume (PLV) maps for liquid penetration characterization.[40] Furthermore, using the RANS approach, we conducted a sensitivity analysis over a range of modeling parameters. We tuned the cone angle (CA), plume direction (PD), and breakup model constants of the framework with the intention of capturing the spray momentum and morphology. The analysis demonstrated an increased sensitivity of the Rayleigh-Taylor size and time constants on liquid penetration and spray collapsing behavior. Despite the systematic calibration effort, the RANS model showed weaker spray collapsing compared to the experiment. Subsequently, the calibrated model parameters were used in a matching LES model, which better captured the plume collapsing phenomena. Our findings suggest that methanol injection can be sufficiently predicted under late-injection stratified DISI conditions, using state-of-the-art high-fidelity LES modeling along with a RANS-driven calibration.

Experimental background: ECN spray M1 methanol

The present study uses the publicly available data from ECN Spray M1 methanol, which resembles stratified late-injection conditions in conventional GDI engines.[23] The experiments deployed a new GDI-style injector consisting of an eight-hole counter-bore configuration[41] operating at an injection pressure of up to 200 bar. Figure 1 illustrates the configuration of the eight-hole injector along with the detailed nozzle topology. The geometrical features of the nozzle, such as the plume direction (PD), serve as input to our simulations and offer a basis for the tuning of the presented modeling approach. The experiments covered a variety of ambient conditions ranging from early-injection flash-boiling at low ambient pressure to late-injection at high ambient pressure and temperature. The details of the replicated ECN experiment are presented in Table 1.

Experimental method

The Spray M experimental campaign was performed by Sandia National Laboratories in their optically accessible constant-flow spray vessel (SV). A detailed explanation of the employed imaging technique and experimental apparatus can be found in a corresponding study by Hwang et al.[24] In particular, the characterization of the spray's liquid phase was conducted by means of projected liquid volume (PLV) using diffused back illumination (DBI) extinction imaging.[42] Using the DBI method, the liquid volume fraction (LVF) can be reconstructed in the three-dimensional space using computer tomography (CT). By measuring the emitted light intensity, the optical thickness of the spray (τ) was calculated, while the resulting PLV can be computed by the following expression:

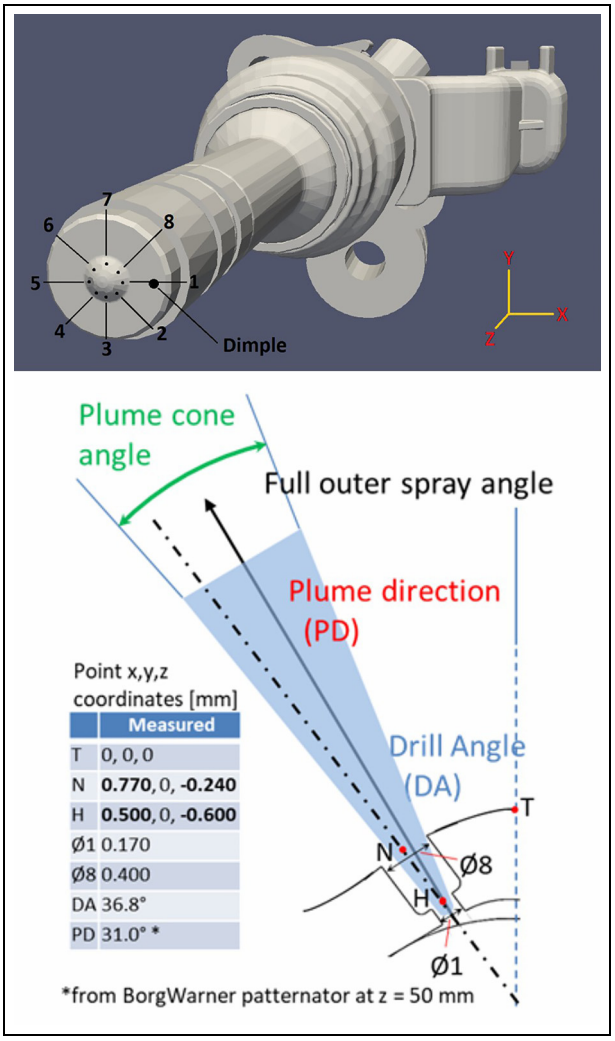

Figure 1. ECN Spray M nozzle geometry.[23]

Table 1. Experimental conditions & injector details for late-injection Methanol Spray M1.

Ambient pressure	6 bar
Ambient temperature	573 K (300°C)
Ambient gas	N_2
Fuel temperature	363 K (90°C)
Injection pressure	200 bar
Injection quantity	mg
Injection duration	0.74 ms
Nozzle diameter	0.170 mm
Counter-bore diameter	0.400 mm
Number of holes	8

$$PLV = \tau \frac{\pi d^3/6}{C_{ext}} = \int_{-y_\infty}^{y_\infty} (LVF)dy, \quad (1)$$

where d is the expected droplet diameter, and C_{ext} is the extinction coefficient. For the expected droplet diameter, we assumed a Sauter mean diameter (SMD) of 10 μm, while we used a C_{ext} of $79.54 \cdot 10^{-6}$mm^2 to estimate the experimental PLV maps. These values were selected according to the ECN guidelines in conjunction with the reported sensitivity analyses from similar condition gasoline and E30 studies.[22–24,37] By setting a threshold to the PLV maps, the experimental results can be directly compared with the CFD results, as will be shown in the following section.

Table 2. Fuel properties.[11,20,24]

Property	Iso-octane	Methanol
Lower heating value (LHV) [MJ/kg]	44.3	20.1
Density (at STP) [kg/m^3]	692	790
Heat of vaporization (at 1 bar) [kJ/kg]	270	1089
Boiling point (at 1 bar) [°C]	99	65
Vapor pressure (at 90°C) [kPa]	70.9	256
Surface tension (at 20°C) [mN/m]	18.6	23
Dynamic viscosity (at 20°C) [mPa · s]	0.5	0.57

Collapsing behavior of methanol spray & comparison with iso-octane

For the Spray G experiments, the ECN used iso-octane as a surrogate for gasoline fuel.[22] Compared to iso-octane, methanol exhibits vastly different physical properties, as shown in Table 2. Mainly, methanol's high latent heat of vaporization, which is four times higher compared to iso-octane, creates an intensive evaporation cooling effect.[11] Considering also the decreased lower heating value, methanol requires up to eight times more thermal energy for the formation of a combustible mixture with similar energy density compared to conventional fuels.[14] Additionally, methanol is more volatile than iso-octane, due to its higher vapor pressure. Thus, methanol evaporates faster than iso-octane while drawing more energy from the surrounding air, due to its latent heat.

These reasons render the fluid mechanics and heat-transfer phenomena of methanol sprays significantly different than the iso-octane spray-cases. Different results were observed experimentally in the same GDI conditions using iso-octane[22] and methanol.[23] In both of the experimental cases, the iso-octane and methanol injection maintained identical injection duration, injected mass, and ambient conditions. Although the two experimental campaigns employed slightly altered injectors, the difference in the results is attributed to the inherent variation of the fuel properties. Specifically, for the same late-injection condition (573 K ambient temperature and 6 bar ambient pressure), while the liquid penetration until the end of injection (EOI) is identical (until 1.3 ms aSOI in Figure 2), methanol evaporation duration is prolonged increasing the liquid residence time in the SV. Although methanol is more volatile due to its high vapor pressure, its high latent heat of vaporization slows the overall evaporation process, as more energy is absorbed from the ambient gas. These two physical properties strongly affect the

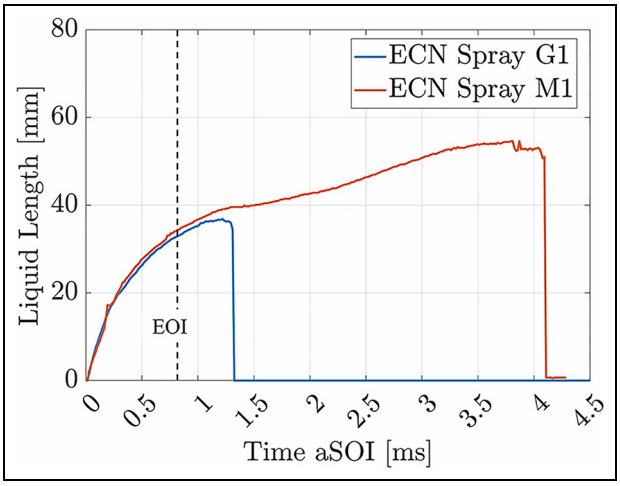

Figure 2. Liquid penetration of Spray G1 & Spray M1.[22,23]

methanol spray morphology, as illustrated in Figure 3. In the methanol case, a strong spray-collapse and sweeping behavior are observed, which merges the spray plumes into a single center-line plume. This phenomenon further increases the evaporation duration due to the smaller effective area for heat transfer between the liquid and the ambient gas. In the corresponding iso-octane experiment, the spray plumes remain intact, while evaporation occurs in faster timescales without interactions between individual plumes. Eventually, the physical properties of methanol, especially its vapor pressure and latent heat, challenges the spray modeling of multi-hole counter-bore injectors.

Methodology

This section introduces the proposed CFD modeling approach, which was developed using the CONVERGE v3.1 CFD software.[39] Our methodology is based on the Lagrangian-Eulerian framework.[43] To model turbulence, we employed both a RANS approach, utilizing the RNG $k-\epsilon$ model,[44] and a LES approach, using the dynamic structure model.[45] To solve the conservation equations, the density-based solver[46] was used in conjunction with the Pressure Implicit with Splitting of Operators (PISO) algorithm.[47] The accuracy of the numerical scheme is first order with respect to time and second order in space. In addition, to calculate the simulation time-step, the Courant-Friedrichs-Lewy (CFL) criterion was used.[39,48] Finally, the thermodynamic properties of methanol and nitrogen were estimated by the Redlich-Kwong equation of state.[49]

Lagrangian spray model

The multiphase modeling approach uses the Lagrangian Particle Tracking (LPT) method to simulate the liquid phase as a set of liquid parcels. For the gaseous phase, consisting of the ambient medium and the evaporated methanol, the Eulerian method is used. The coupling between the liquid and gaseous phase is secured through the exchange of mass, momentum, and energy with respective source terms in the transport equations.[43] In the LPT technique, the parcels require an extra set of phenomenological models that describe sub-grid fluid phenomena such as breakup, collisions, evaporation, and turbulence effects. It should be noted that the presented Lagrangian-Eulerian framework is specifically applicable for liquid fuels injected in conditions outside of the flash-boiling regime.

The computational parcels are initially injected using the Reitz and Diwakar model.[50] The injection model treats the droplets as 'blobs' with an initial diameter equal to the effective nozzle diameter. Subsequently, the parcels experience breakup due to flow instabilities originating from their interaction with the ambient gas. We used the combined wave model,[51] which employs Kelvin-Helmholtz (KH) and Rayleigh-Taylor (RT) hydrodynamic instabilities to calculate the timescales and length-scales for the resulting droplets (more information in the following section). Moreover, the No Time Counter (NTC) algorithm[52] was used to predict the parcel collisions. We also used the model of Post and Abraham[53] to calculate the post-collision outcomes encompassing bouncing, stretching, reflective separation, and coalescence.

To ensure the interaction of the parcels with the ambient gas, we used additional models for the aerodynamic drag forces and the turbulent phenomena. The aerodynamic drag force was calculated using the dynamic drag model, which considers the droplet distortion for calculating the drag coefficient.[54] Specifically, to consistently calculate the drag coefficient, the dynamic drag model uses the Taylor Analogy Breakup (TAB) model to estimate the droplet distortion. The effects of turbulence were regarded using the turbulent dispersion model of O'Rourke.[55] Lastly, the Frossling-correlation-based evaporation model was used to calculate the droplet evaporation, which assumes a uniform temperature profile within each parcel.[46] The summary of the adopted spray models is presented in Table 3.

Droplet breakup model

As mentioned in the previous section, the KH-RT model is adopted for the droplet breakup of the injected methanol.[51] For better agreement with the experiment, the breakup length of the model was set as zero to enable the competition between the KH and RT breakup immediately as each parcel exits the counter-bore region.[37] Additionally, we also tested the modified KH-RT model by Patterson and Reitz,[56] which does not require a breakup length for the activation of the RT model. Similarly, with a previous ECN Spray G study,[34] this modified model under-predicted the liquid penetration and, therefore, the Beale and Reitz and Beale model[51] was selected as the most appropriate for our study. The inherent distinction between these two models lies in the need to input a

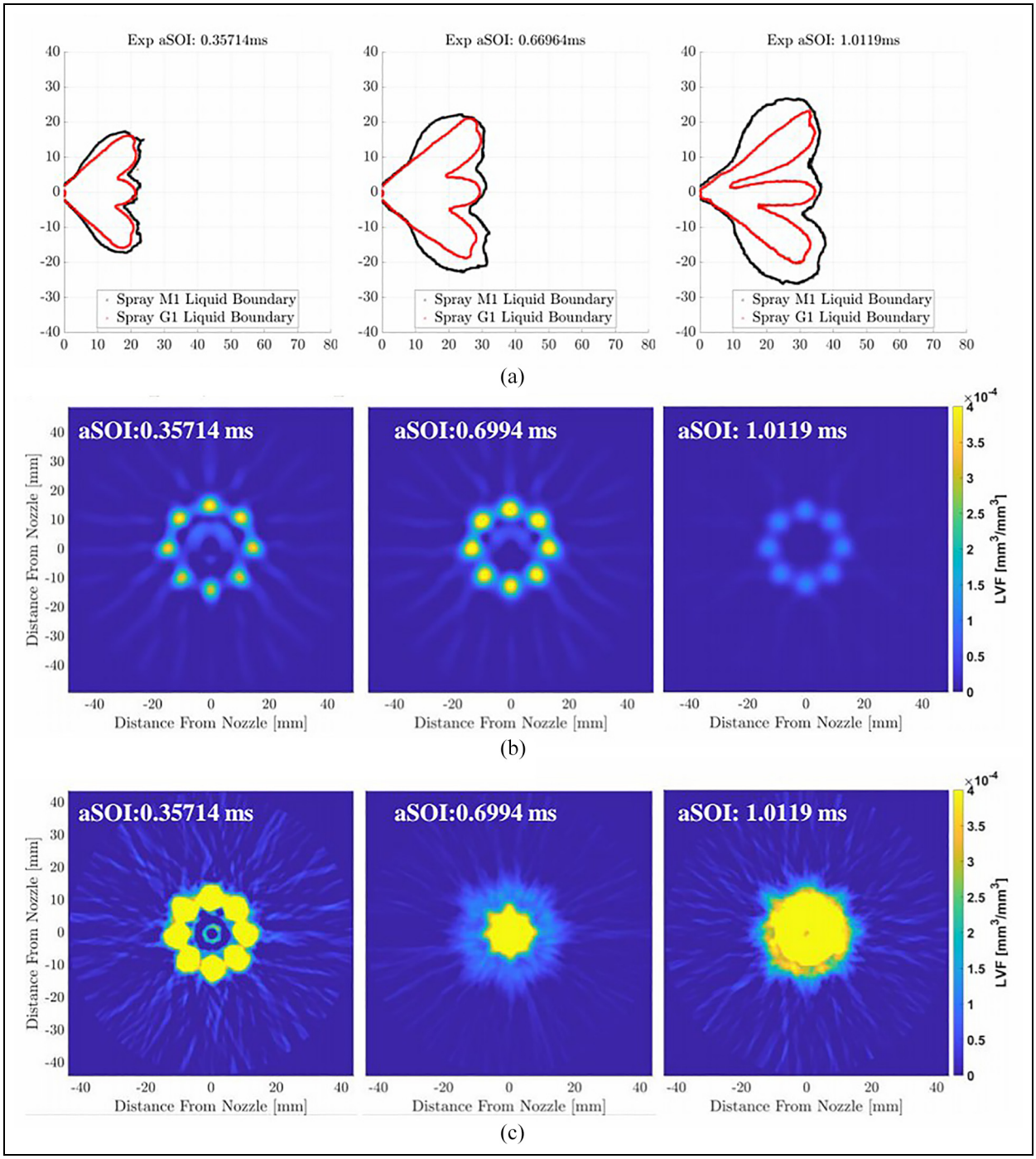

Figure 3. Spray G1 & Spray M1: (a) experimental comparison of projected Liquid boundary measured by DBI extinction imaging with extinction threshold set as $0.2 \cdot 10^{-3} mm^3(\text{liquid})/mm^2$, (b and c) LVF at perpendicular XY-plane of the injection direction - z = 15 mm distance from nozzle exit.[22,23]

predefined breakup length. The Reitz and Beale model[51] requires a predefined breakup length to establish the onset of competition between KH and RT mechanisms. In contrast, the Patterson and Reitz model[56] calculates the breakup process directly without relying on a predefined length. This approach proves inaccurate for our case, as the Patterson and Reitz model first determines the occurrence of RT instability before testing whether the KH instability criterion is met. Thus, the potential fulfilment of RT breakup omits the KH breakup criterion while favoring the RT breakup. On the contrary, the Beale and Reitz model simulates a concurrent competition between the two mechanisms.

The Kelvin-Helmholtz hydrodynamic instabilities result from unstable shear waves growing between the high velocity liquid spray surface and the ambient gas. If these surface waves grow for a sufficient time, they cause liquid detachment from the parcels and, eventually, form smaller new parcels. The newly formed child

Table 3. Numerical models.

Physical phenomena	Numerical models
Fluid flow	Navier Stokes, density-based solver[46]
Turbulence	RNG $k-\epsilon$ model 44 & LES Dynamic Structure model[45]
Droplet injection	Blob model[50]
Droplet breakup	KH-RT model[51]
Droplet drag force	Dynamic Drag Model[54]
Droplet collision	NTC model[52]
Droplet coalescence	Post Collision Outcome model[53]
Droplet turbulent dispersion	O'Rourke[55] model
Droplet evaporation	Frossling correlation-based & boiling model[46]

parcels have a radius r_c, which is proportional to the wavelength of the instability, and is calculated by the following expression[51]:

$$r_c = B_0 \Lambda_{KH}, \tag{2}$$

where Λ_{KH} is the wavelength of the fastest growing wave, and B_0 is the KH model size constant. The decreasing parent parcel radius r_p can be estimated as follows:

$$\frac{dr_p}{dt} = -\frac{(r_p - r_c)}{\tau_{KH}}, \tag{3}$$

where the breakup time τ_{KH} is established as:

$$\tau_{KH} = \frac{3.726 B_1 r_p}{\Lambda_{KH}\,\Omega_{KH}}, \tag{4}$$

where B_1 is the breakup time constant, and Ω_{KH} is the growth rate of the Λ_{KH} wavelength. Moreover, after droplet breakup, the child parcels accumulate liquid mass from the parent parcel. To estimate the accumulated mass, a shed factor s is used, which determines the fraction of the mass of the parent parcel that is transferred to child parcels.

Furthermore, the RT model is based on Rayleigh-Taylor hydrodynamic instabilities which occur due to deceleration of the high speed liquid jet exiting the nozzle. This deceleration also causes unstable waves, which are perpendicular to the spray tip and cause droplet breakup.[51] Breakup occurs once the wavelength scale ($C_{RT}\,\Lambda_{RT}$) becomes smaller than the diameter of the parent droplet, and given that the RT waves have grown on the droplet surface for a period longer than the breakup time. Similarly with the KH model, the RT breakup time τ_{RT} is calculated by the following equation:

$$\tau_{RT} = \frac{C_\tau}{\Omega_{RT}}, \tag{5}$$

where C_τ is the RT breakup time constant, and Ω_{RT} is the fastest wave growth rate. The resulting child droplet radius r_c is given by the following expression:

$$r_c = \frac{C_{RT}\Lambda_{RT}}{2} \tag{6}$$

Computational domain & mesh

To accommodate the numerical calculations, we generated a cylindrical geometry to replicate the SV conditions of the ECN Spray M experiment (Figure 4). For the cylinder dimensions, we used a radius of 54 mm and height of 83 mm, which were defined according to previous modeling practices of ECN sprays.[14,36,37,57] The cylinder boundary conditions were assigned as wall-type Dirichlet for the temperature and Neumann for the turbulent kinetic energy. The wall temperature was set as 573 K, similar to the ambient temperature of the constant-flow SV. For the grid generation, we employed the CONVERGE cut-cell Cartesian method[46,58] using a base cell size of 2 mm for the RANS simulations, and 1.3 mm for the LES cases.

To obtain a higher fidelity mesh, we applied fixed embedding in areas of interest, while the adaptive mesh

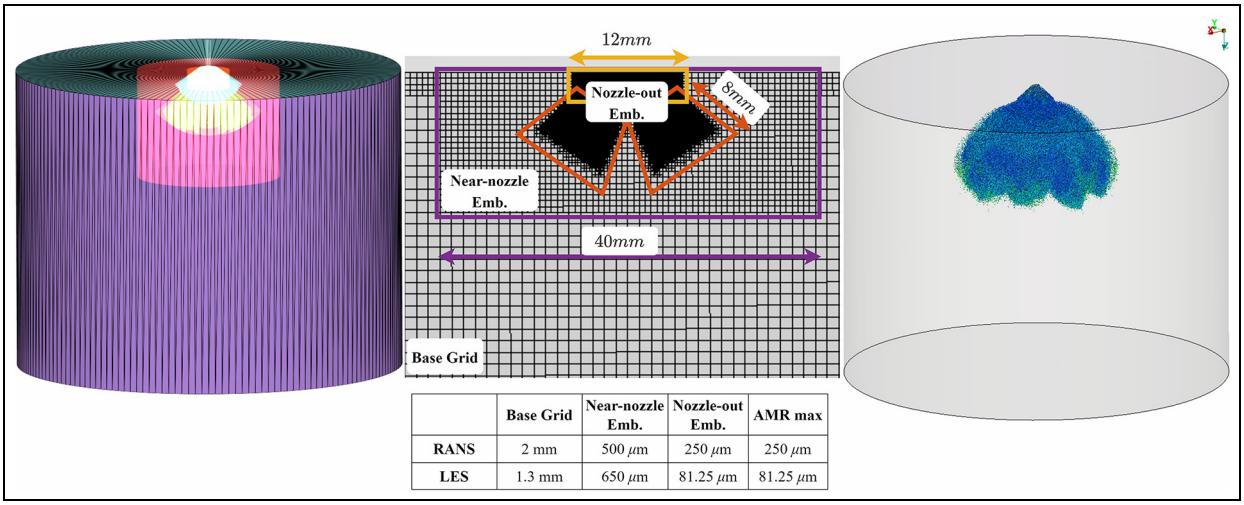

	Base Grid	Near-nozzle Emb.	Nozzle-out Emb.	AMR max
RANS	2 mm	500 μm	250 μm	250 μm
LES	1.3 mm	650 μm	81.25 μm	81.25 μm

Figure 4. Computational domain for the constant-flow spray vessel, the employed mesh grid strategy, and the Lagrangian parcels.

Table 4. Model settings.

Breakup model	
KH Model size & breaksup time constants	$B_0 = 0.6, \quad B_1 = 50$
KH Shed factor	$s = 0.5$
RT Model size & breaksup time constants	$C_{RT} = 0.6, \quad C_\tau = 0.5$
RANS turbulence model	
RNG $k-\epsilon$ constants	$C_\mu = 0.0845, \quad C_{\epsilon 1} = 1.42, \quad C_{\epsilon 2} = 1.68, \quad C_{\epsilon 3} = -1.0$
Initial turbulence intensity	
Turbulent Kinetic Energy (TKE)	$k_0 = 6.4 \cdot 10^{-3} m^2/s^2$
TKE Dissipation Rate	$\varepsilon_0 = 5.08 \cdot 10^{-1} m^2/s^3$ (for the RANS model only)
Mass diffusivity	
Methanol diffusivity constants	$D_0 = 1.336 \cdot 10^{-5}, \quad n_0 = 1.8$

refinement (AMR) algorithm was used for automatic refinements on the basis of velocity and methanol species gradients. Three different types of fixed embedding were used, two in the nozzle-out region, and one in the outer near-nozzle area. To resolve the nozzle-out flow, a spray-cone and a cylindrical-style refinement were utilized accomplishing a grid size of 250 μm for the RANS, and 81.25 μm for the LES simulations. On the other hand, the near-nozzle region was refined in a cylindrical-style using a grid size of 500 μm for the RANS, and 650 μm for the LES simulations to avoid excessive computational costs. The details of the meshing strategy are presented thoroughly in Figure 4. Regarding the AMR strategy, in the RANS cases, the maximum embedding level was set as 3 leading to a minimum cell size of 250 μm. The adopted meshing strategy aligns with similar iso-octane and E30 study using multi-hole counter-bore injectors[37] For the LES simulations, we set a maximum embedding level of 4, obtaining a minimum cell size of 81.25 μm. Finally, the sub-grid embedding criterion for the AMR was set as 0.1 m/s for velocity refinement and 0.001 methanol mass fraction for species refinement. Based on the numerical predictions, the adopted meshing strategy was deemed trustworthy and robust in terms of numerical accuracy and computational cost.[58]

Numerical model settings

The complete settings of the presented numerical framework are depicted in Table 4. To obtain a realistic value for the turbulence conditions prior to injection, we used the available ECN spray G particle-image-velocimetry (PIV) measurements to estimate the initial turbulent intensity inside the constant-flow SV.[22] As a result, more realistic predictions were achieved as the methanol experimental campaign used the same conditions as the Spray G experiments. A sensitivity analysis on the initial turbulence intensity can be found in the study of Bestel et al.[37]

For the calculation of liquid penetration, we used the new ECN liquid penetration length definition.[40] The computational results were post-processed using a set of ECN-provided python scripts,[21] which calculate the PLV maps by projecting the liquid volume fraction (LVF) across the y-direction. Using the PLV maps, the ECN recommends using a 'low' and a 'high' threshold for the comparison with the experimental data. These thresholds are calculated as follows:

$$PLV = \int_{-y_\infty}^{y_\infty} (LVF)dy = 0.2 \cdot 10^{-3} \frac{\text{mm}^3(\text{liquid})}{\text{mm}^2} \qquad 2.0 \cdot 10^{-3} \frac{\text{mm}^3(\text{liquid})}{\text{mm}^2} \tag{7}$$

In our study, we used the 'low' threshold $0.2 \cdot 10^{-3}$ to plot the liquid boundary and, subsequently, compare it with the corresponding computer tomography LVF results. A visual representation of the CFD post-processing procedure and comparison with the experiments is illustrated in Figure 5.

Injector nozzle parameters

Table 5 depicts the nozzle parameters which were used for the present study. Compared to iso-octane, methanol exhibits a higher vapor pressure and lower boiling point (Table 2), which increases the probability of methanol vapor in the nozzles. As a result, under similar conditions, cavitation phenomena might be increased during methanol injection, leading to a smaller effective nozzle area and higher initial jet momentum. Previous in-nozzle flow[59] and LPT[34,35] simulations using the spray G nozzle used a discharge coefficient value of 0.4815 and 0.5 respectively. In our study, to account for this augmented methanol in-nozzle cavitation, we set the discharge coefficient C_d as 0.47 to match the initial momentum of the liquid jet based on a sensitivity study.

Due to the absence of the nozzle geometry file, the injected parcels were initialized at the counter-bore exit (N in Figure 1) rather than the nozzle-exit location (H in Figure 1). This technique was proven valid by Kumar and Van Dam,[34] who compared different injection locations for the spray G nozzle. They stated that adequate predictions can be obtained by using the counter-bore

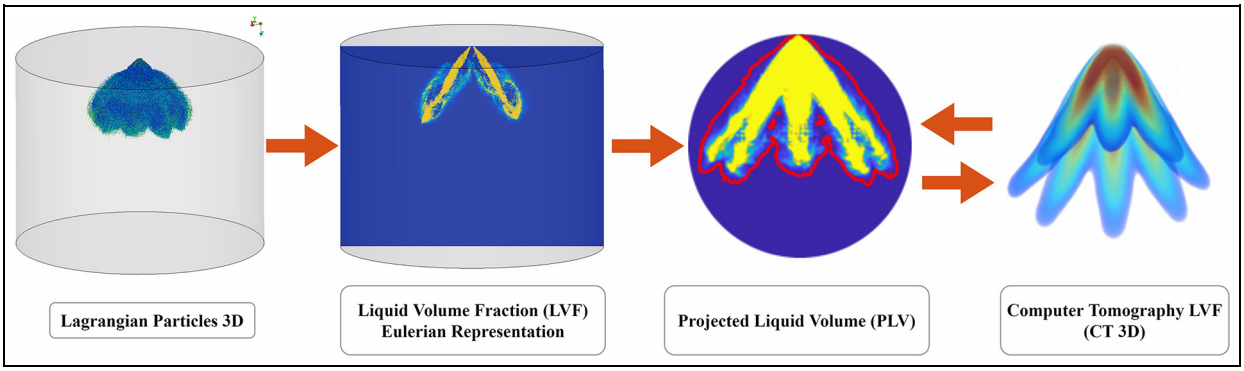

Figure 5. Calculation of liquid penetration and comparison with experimental DBI data.[24,36]

Table 5. Used nozzle parameters for ECN Spray M1 numerical framework.

Discharge coefficient	$C_d = 0.47$
Velocity coefficient	$C_v = 0.80$
Cone angle	33°
Plume direction	34°
Number of parcels per nozzle	RANS: 70000, LES: 150000

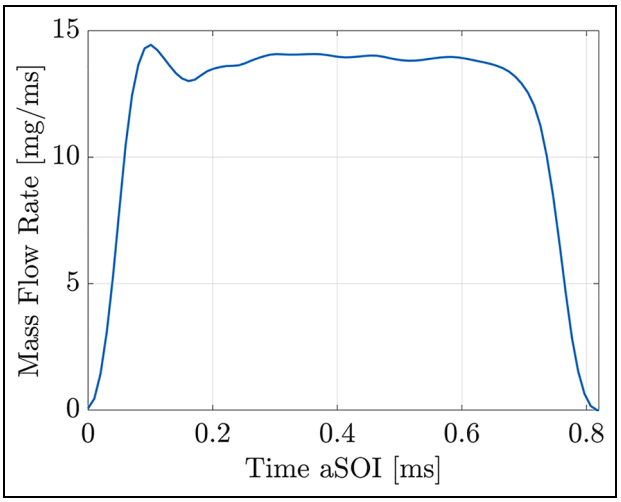

Figure 6. Injection rate profile for ECN Spray M injector using methanol.[23]

exit injection-location along with the experimentally measured mass flow rate-of-injection (ROI) profile. Moreover, we used the Spray M1 ROI profile (Figure 6), which is provided by ECN.[23] Lastly, similarly to the iso-octane study of Bestel et al.,[37] the parcels were injected using a uniform distribution, which equally allocates the parcels across the spray plumes.

Results

Our study adopted a structured simulation plan to investigate the predictive capabilities of the presented framework. Initially, using the RANS turbulence approach, we performed a set of simulations altering the KH-RT breakup constants. By assessing the impact of each breakup constant individually, we selected the best performing constants and calibrated our model for methanol injection. Consequently, the calibrated model was compared with a corresponding LES model using the same breakup constants. Lastly, in the appendix, an evaluation of the plume cone angle sensitivity is presented for both the calibrated RANS and LES models.

Assessment of KH-RT breakup model constants

Influence of KH time constant & shed factor. This section covers the parametric investigation for the KH model time constant B_1 and shed factor. These values were altered independently each time to evaluate their individual impact on the methanol spray. The parametric sweep was systematically performed to ensure physically accurate values that adhered to mass and momentum conservation. Thus, the KH model time constant B_1 ranged from 10 to 50 inducing fast to slow KH breakup occurrence. The shed factor ranged from 0.1 to 1.0 representing 10% to 100% of the parent parcel mass transferred to child parcels. The RT model parameters were kept constant according to the baseline modeling framework that was presented in Table 4. For all of the presented liquid plots, the 'low' threshold $0.2 \cdot 10^{-3}$ was imposed on the generated PLV maps according to ECN guidelines.

Based on the KH model formulation presented in the previous section, increasing the B_1 constant amplifies the KH breakup time τ_{KH}, which in turn, decreases the breakup rate and the KH breakup occurrence. Figure 7 presents the spray liquid penetration, and liquid width for a range of KH time constants. The spray liquid width is plotted for two axial cross-sections at 15 and 25 mm downstream distance from the nozzle tip. Moreover, increasing the B_1 constant does not significantly affect the liquid penetration. Contrary to that, we observe a minor increase in the 15 mm cross-section liquid width, which aligns better with the experimental liquid width. The spray morphology was also similar for all tested parameters, indicating minor impact from the time constant calibration.

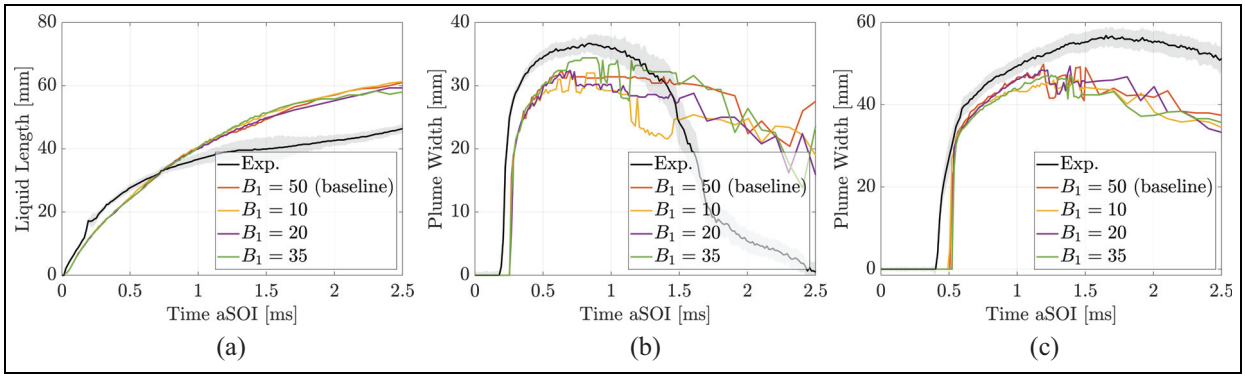

Figure 7. Impact of KH time constant on liquid penetration & width using the RANS modeling approach: (a) KH time constant sensitivity on liquid penetration length, (b) KH time constant sensitivity on liquid width at $z = 15$ mm axial cross-section from nozzle exit, and (c) KH time constant sensitivity on liquid width at $z = 25$ mm axial cross-section from nozzle exit

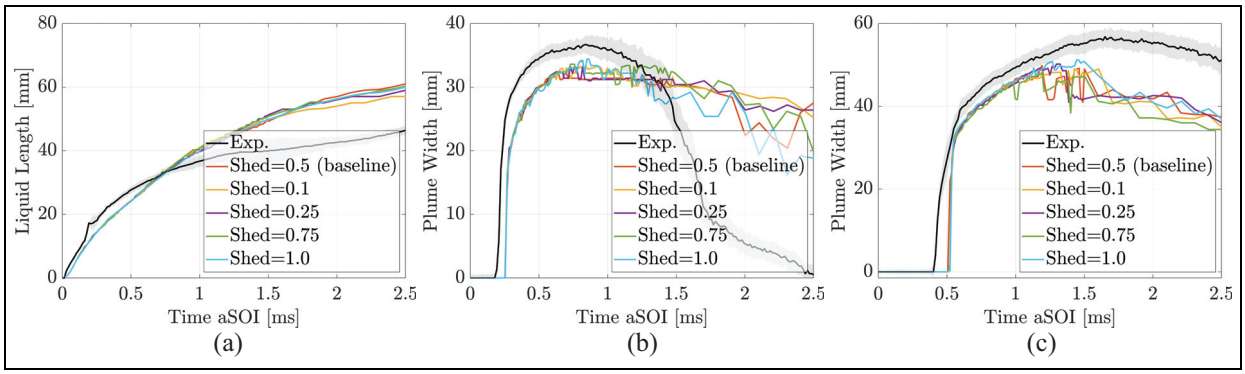

Figure 8. Impact of KH shed factor on liquid penetration & width using the RANS modeling approach: (a) KH Shed factor sensitivity on liquid penetration length, (b) KH shed factor sensitivity on liquid width at $z = 15$ mm axial cross-section from nozzle exit, and (c) KH shed factor sensitivity on liquid width at $z = 25$ mm axial cross-section from nozzle exit

On the other hand, increasing the shed factor leads to higher mass fractions in the resulting child parcels after KH breakup occurrence. The influence of the shed factor in liquid penetration and width is shown in Figure 8. While the impact on liquid length is negligible, the shed factor 1.0 model captures better the spray width evolution until the 1.5 ms after the start of injection (aSOI) point. The spray width remains constant in the later stages after the EOI, contrary to the experimental observations where a decrease is noted. This could possibly be attributed to accumulated droplets in the spray plume tips, which cause decreased evaporation (discussed in the following section). The difference in the qualitative comparison in the LVF distribution is negligible and, therefore, is not presented here. In conclusion, in the present RANS model, the global liquid penetration and width results are insensitive to the alteration of the B_1, while a shed factor of 1.0 gives a slightly improved prediction of the spray width.

Influence of RT size & time constant. The RT model constants were investigated based on their impact on the global spray results. Similarly with the KH model, the RT time constant C_τ determines the breakup time τ_{RT} and the RT breakup occurrence. Further, the RT size constant C_{RT} influences the size of the child parcels after the RT breakup. Increased values of the C_{RT} are expected to increase the spray momentum in the later stages after the EOI due to the delayed evaporation by the larger child parcels. Both of the investigated RT model constants ranged from 0.1 to 1.0, complying with recommended values.[46] This influence on liquid penetration and width is confirmed by Figure 9. For lower values of C_{RT}, the liquid length increases steeply until 1.7 ms, where the extremely small droplets evaporate abruptly, causing a massive decrease in liquid length. The initial increase in penetration can be attributed to the smaller drag force acting on the parcels due to their decreased diameter. Furthermore, the liquid width is massively under-predicted, which confirms the augmented evaporation occurring on the periphery of the spray plumes.

For the lower C_{RT} values, abrupt evaporation and narrower plume morphology are also highlighted by the comparison with the experimental liquid boundary in Figure 10. Increased C_{RT} values demonstrate a better agreement with the experimental liquid boundary,

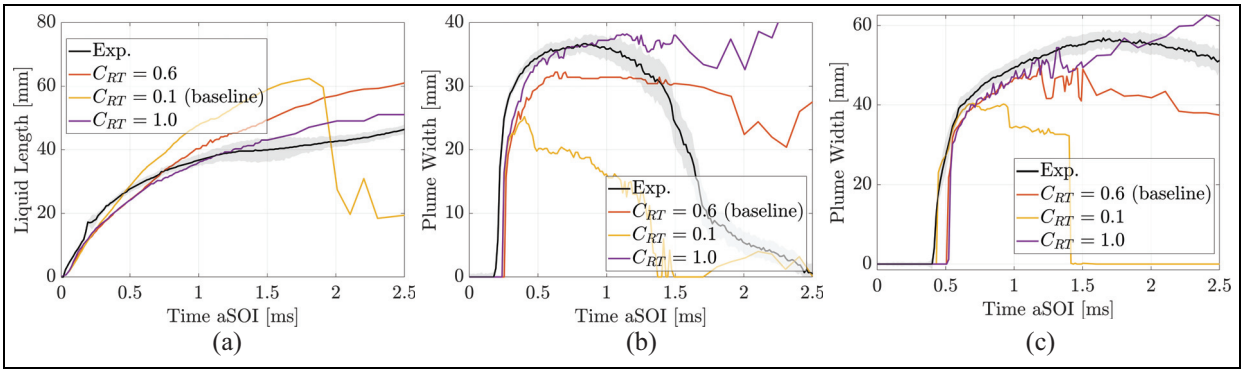

Figure 9. Impact of RT size constant on liquid penetration & width using the RANS modeling approach: (a) RT size constant sensitivity on liquid penetration length, (b) RT size constant sensitivity on liquid width at z = 15 mm axial cross-section from nozzle exit, and (c) RT size constant sensitivity on liquid width at z = 25 mm axial cross-section from nozzle exit

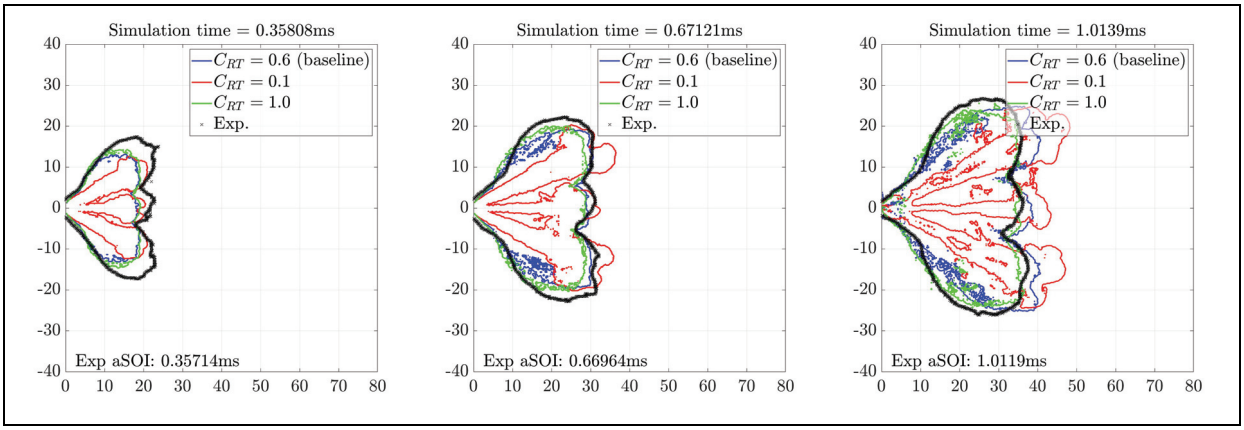

Figure 10. Liquid boundary derived by means of projected liquid volume (PLV) maps: Comparison for different C_{RT} values.

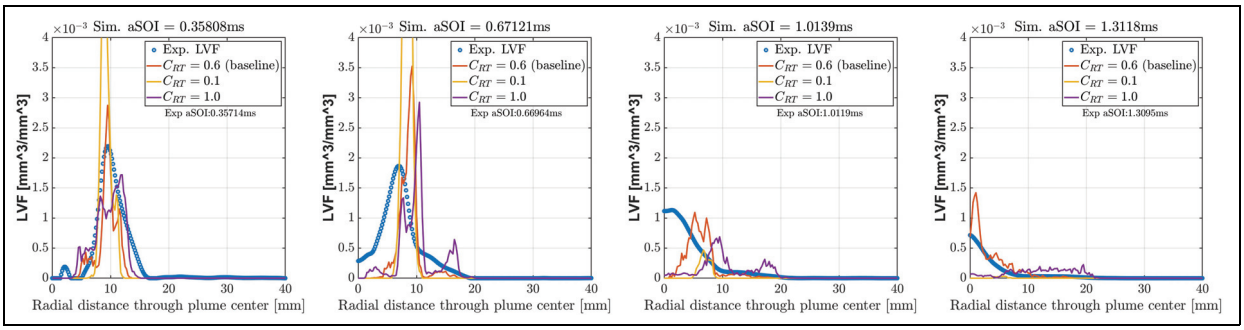

Figure 11. Quantitative plume-averaged Liquid Volume Fraction (LVF) at z = 15 mm axial cross-section from nozzle exit: Comparison for different C_{RT} values.

liquid length and liquid width. Figure 11 depicts the plume-averaged LVF in the radial direction, which is perpendicular to the spray axis and at a distance of 15 mm downstream from the injector tip. The narrower plumes exhibit an accumulation of liquid in the center of the plume, which causes an over-prediction of the LVF. Using a C_{RT} value of 1.0 creates a wider plume, which quantitatively adequately matches the experimental LVF during the spray formation stages before the EOI. During the later stages of the spray formation, the plume collapsing phenomenon, highlighted by the accumulation of LVF in the spray center-line axis, is not predicted adequately by the C_{RT} = 1.0 model. This reveals the weakness of the RANS model in capturing both the correct liquid length and the spray collapsing behavior of methanol.

A similar trend is also observed in the parametric investigation of the RT time constant. Increasing the C_τ constant in Figure 12 leads to delayed RT breakup occurrence. Subsequently, the liquid length decreases,

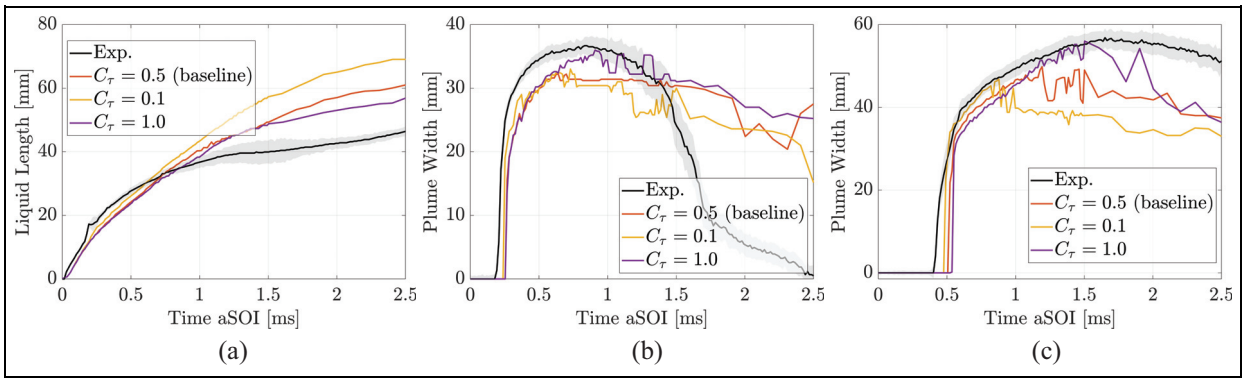

Figure 12. Impact of RT time constant on liquid penetration & width using the RANS modeling approach: (a) RT time constant sensitivity on liquid penetration length, (b) RT time constant sensitivity on liquid width at $z = 15$ mm axial cross-section from nozzle exit, and (c) RT time constant sensitivity on liquid width at $z = 25$ mm axial cross-section from nozzle exit

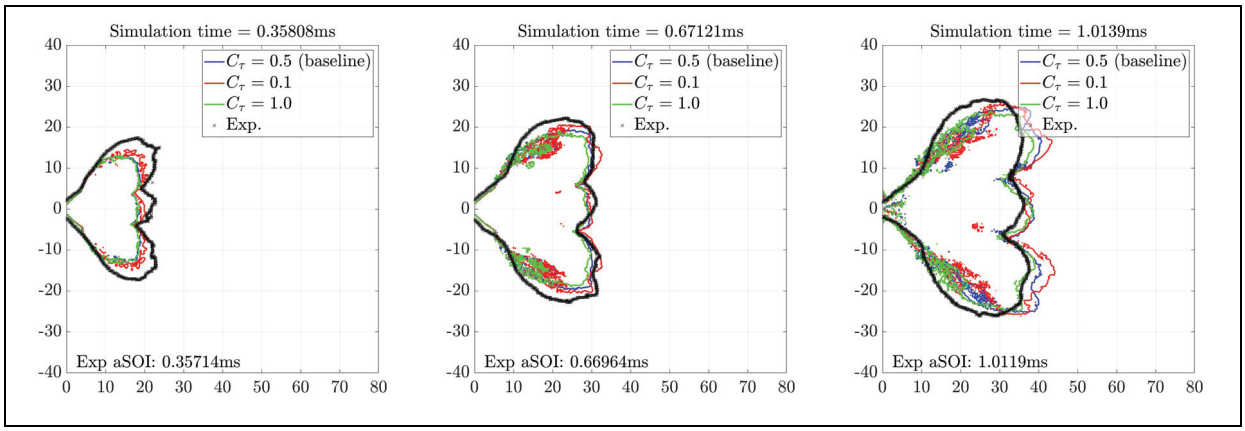

Figure 13. Liquid boundary derived by means of projected liquid volume (PLV) maps: Comparison for different C_τ values.

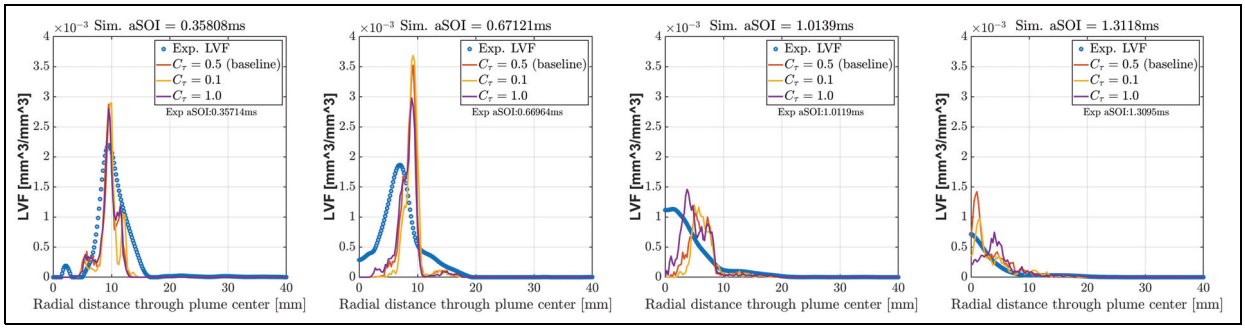

Figure 14. Quantitative plume-averaged liquid volume fraction (LVF) at $z = 15$ mm axial cross-section from nozzle exit: Comparison for different C_τ values.

while the model captures more adequately the spray outward expansion. In Figure 13, despite the over-prediction in liquid length, the spray morphology and the liquid width is similar to the experimental plume morphology. The LVF in the radial direction is presented in Figure 14 for the tested range of C_τ constants. For a C_τ value of 1.0, spray collapsing is diminished, while the accumulation of liquid in the center of the plume decreases. This strongly indicates the significant influence of the RT model on spray penetration, spray morphology, and plume collapsing. Increasing both the RT size and time constants leads to a better agreement in the spray momentum (i.e. liquid length and liquid width) and the spray morphology. However, smaller values of the constants inflict a more pronounced spray collapsing, which is typical of the methanol injection ECN experiment. To more precisely tune these parameters, near-nozzle and Sauter Mean Diameter (SMD)

Table 6. Overview of baseline and calibrated KH-RT breakup constants.

Constant	Baseline	Calibration
KH Time Constant B_1	50	50
KH Shed Factor s	0.5	1.0
RT Size constant C_{RT}	0.6	1.0
RT Time constant C_τ	0.5	1.0

measurements are required to accurately capture both the initial spray momentum and post-injection phenomena, including the plume collapsing and the subsequent outward spray sweeping.

RANS spray model calibration

Based on the evaluation of the KH-RT constants, we ran a calibrated RANS model combining the best performing parameters. For the KH constants, we maintained the same value for the time constant as it demonstrated minimal contribution to the spray results. Similarly, with the study of Bestel et al.,[37] the shed factor was increased to 1.0 due to its potential to capture the spray morphology better. Furthermore, the tuning of the RT model was more impactful as both the size and time constants significantly affected the simulated methanol spray. Based on the available experimental LVF measurements, we determined a value of 1.0 for both of these constants, enabling accurate capture of liquid penetration, liquid width, and spray morphology. In Table 6, we present an overview between the baseline and the calibrated breakup constants. Interestingly, the optimal parameters closely align with the iso-octane and E30 study by Bestel et al.,[37] indicating that Lagrangian breakup models are sufficiently versatile for methanol injection.

Figure 15 illustrates the liquid penetration and liquid width of the calibrated RANS model, the initial baseline, and the experimental results. Compared to the baseline model, the calibrated case predicts liquid penetration more adequately with a smaller over-shoot in the later stages after the EOI. In the initial injection stages, both models under-predicted liquid penetration, highlighting a disparity in the predicted spray momentum. Further reducing the discharge coefficient could aid in capturing the initial spray momentum and replicate potential in-nozzle methanol effects. However, to consistently improve the present model, additional experiments are required to determine the discharge and velocity coefficients. In-nozzle VoF simulations could also identify the methanol cavitation phenomena and enhance the predictive capabilities of the presented approach.

Concerning the liquid width, during the initial stages of the simulation, the calibrated model successfully recreated the experimental maximum spray width. The improved spray morphology is presented in Figure 16. The calibrated model finely captured the plume morphology and the outward expansion motion typical of methanol multi-hole spray. Similar to liquid length, after 1.5 ms aSOI, the spray width is over-predicted for both RANS models. This behavior indicates the presence of slowly evaporating droplets in the tip of the spray plumes, which locally increase the LVF of the simulations. This is confirmed by Figure 17, where the radial LVF is greater than zero in the outer regions of the spray, even for the $z = 15$ mm cross-section.

Figure 18 depicts the LVF distribution in the XY-plane at the 15 mm distance from the injector tip. The presented RANS models adequately captured the qualitative and quantitative (Figure 17) distribution for the initial injection stages. However, during the later stages, methanol demonstrated a strong plume collapsing behavior typical of flash-boiling gasoline sprays.[60] In the corresponding models, this tendency of the plumes to move toward the center is severely under-predicted by all simulation cases. Furthermore, before the EOI, the calibrated RANS model exhibited a faster collapse and improved morphology compared to the baseline model. After the EOI, the baseline model showed improved plume collapsing, and increased LVF values

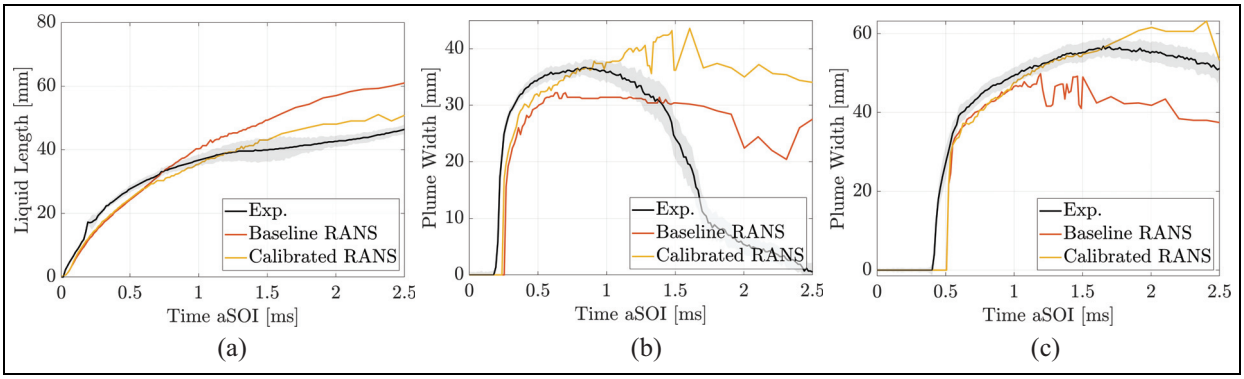

Figure 15. Comparison between baseline & calibrated RANS models: Liquid penetration & width: (a) Comparison between baseline & calibrated RANS models: Liquid penetration length, (b) Comparison between baseline & calibrated RANS models: Liquid width at $z = 15$ mm axial cross-section from nozzle exit, and (c) Comparison between baseline & calibrated RANS models: Liquid width at $z = 25$ mm axial cross-section from nozzle exit

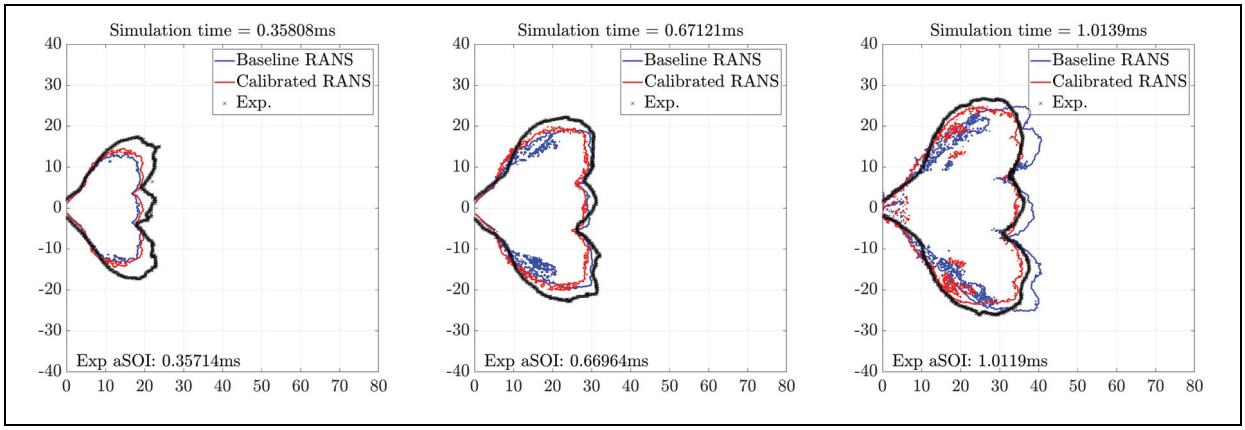

Figure 16. Liquid boundary derived by means of projected liquid volume (PLV) maps: Comparison between baseline & calibrated RANS models.

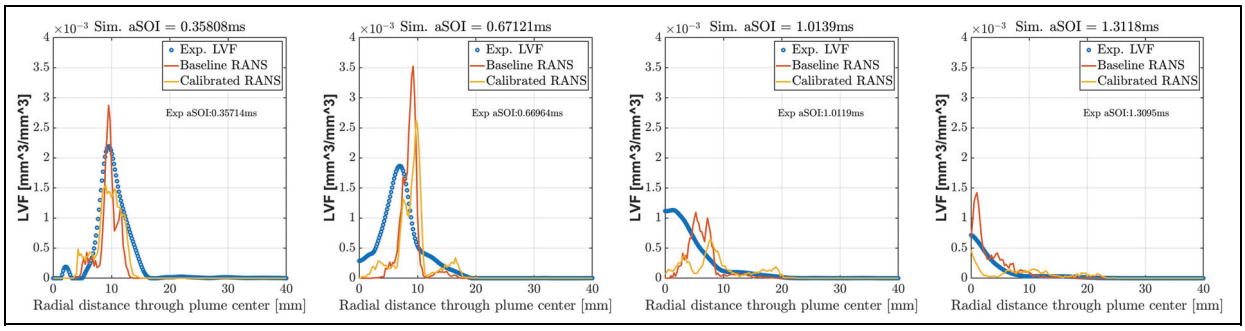

Figure 17. Quantitative plume-averaged liquid volume fraction (LVF) at $z = 15$ mm axial cross-section from nozzle exit: Comparison between baseline & calibrated RANS models.

in the spray center-line (1.0119 ms simulation time in Figure 17). Potentially, in the later stages after the EOI, this accumulation of liquid mass caused the over-prediction of the liquid penetration due to decreased evaporation rates. Despite having acceptable predictions of the liquid length and the morphology, these outlined discrepancies expose a weakness of the RANS approach in capturing the underlined physical phenomena. As a result, the spray plume collapsing, although partially replicated by the model, is weak compared to the experiments.

LES model results & comparison with RANS approach

A LES turbulence approach was implemented using the calibrated spray model settings from the RANS study to capture post-injection phenomena better. While RANS modeling is commonly preferred in CFD practices for automotive, heavy-duty and maritime engines, it is scientifically valuable to explore whether the observations would differ when modeling the present spray using LES. Thus, the scope of the simulation was to capture the experimentally observed plume collapsing phenomenon while maintaining adequate predictions of the spray momentum and morphology. For comparison, we also ran an extra LES simulation using the baseline KH-RT constants. Figure 19 presents the liquid penetration and spray plume width results for the LES models. The calibrated LES model demonstrated slightly improved predictions for the liquid penetration compared to the RANS approach. In the 15 mm cross-section plume width, a major improvement was achieved by the LES model, which successfully recreated the declining plume width trend after 1.5 ms aSOI. This indicates that the LES model can effectively reproduce the designated methanol injection phenomena.

Figure 20 illustrates the plume-averaged LVF in the radial direction at 15 mm downstream distance from the injector tip. In the initial stages of injection, the calibrated LES model matches satisfactorily with the experimental LVF distribution. During the EOI, at 0.669 64 ms time aSOI, all of the simulations fail to match the LVF due to the mismatch in the spray momentum. Following the end of injection, both LES models effectively capture the evolution of spray plume collapse and sweeping motion. In contrast, the RANS model underestimates the LVF accumulation along the spray center-line, whereas the LES models successfully capture this phenomenon.

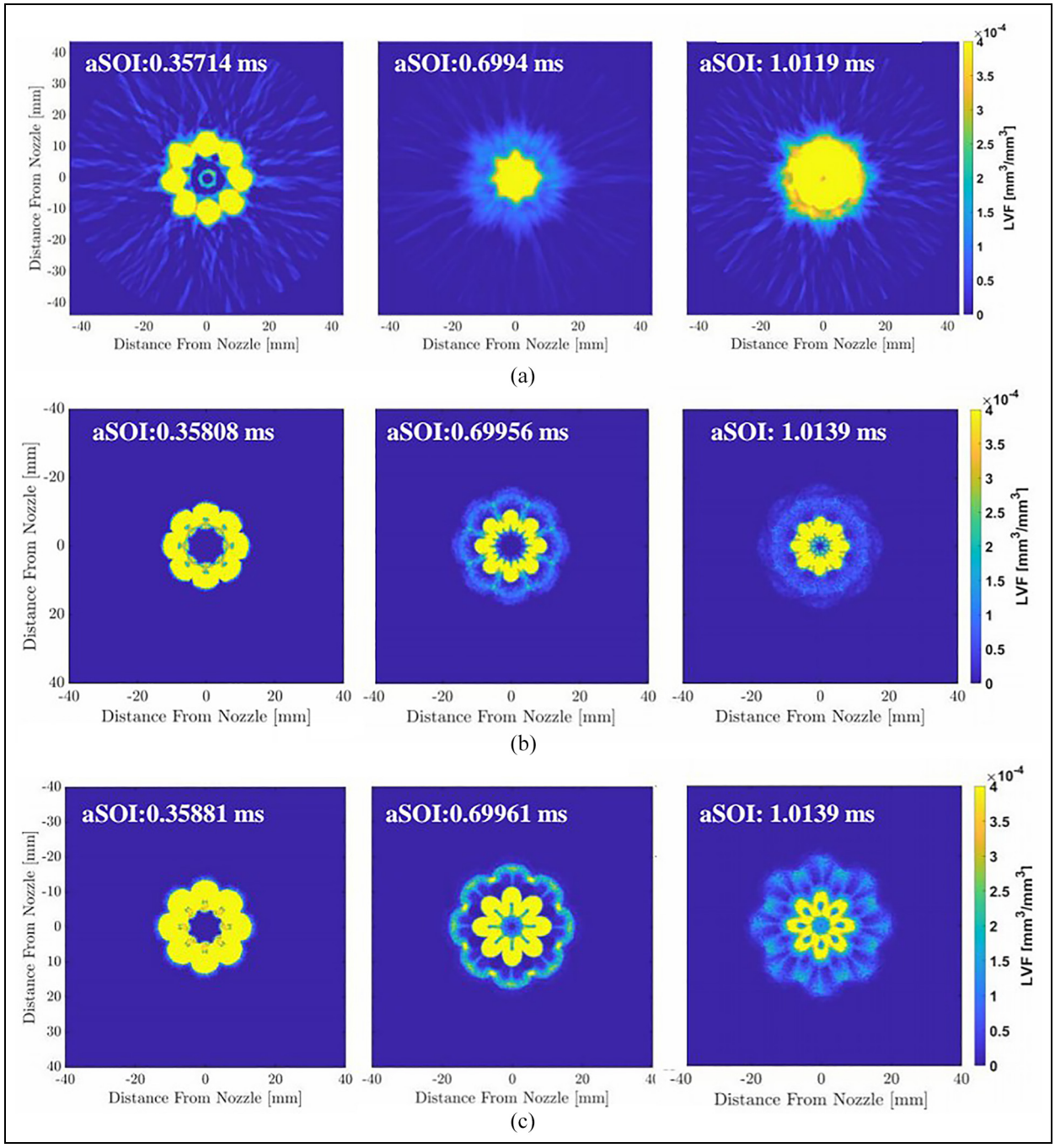

Figure 18. Qualitative XY-plane Liquid Volume Fraction (LVF) distribution at $z = 15$mm axial cross-section from nozzle exit: Comparison between Experimental LVF (a), Baseline RANS Model (b) & Calibrated RANS Model (c).

Figure 21 compares the XY-plane LVF distribution between the LES models and the experiment results. Both LES models present an improved prediction of the plume collapsing compared to the RANS models in Figure 18. Even in the baseline LES model, the plumes' tendency to move toward the center is more pronounced, suggesting that LES can provide accurate predictions without the need for extensive tuning. Utilizing the RANS-calibrated KH-RT model constants revealed that even more accurate predictions could be achieved in the final LES simulation.

Finally, Figure 22 presents the qualitative YZ-plane cross-section LVF distribution along the injection axis. This visualization allows for comparing plume geometry evolution between the calibrated RANS and LES models, as well as the experimental data. The LES model exhibits a more pronounced accumulation of liquid along the spray center-line, confirming the improved spray collapsing compared to the RANS model. Both approaches over-predict the liquid volume fraction (LVF) at the spray plume tips. This effect is more intense in the RANS model, while the LES model

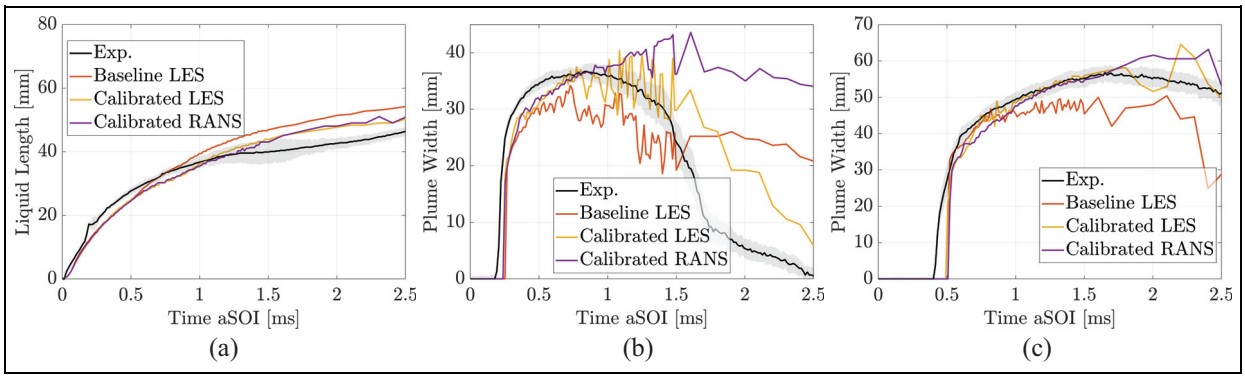

Figure 19. Comparison between LES & RANS models: Liquid penetration & width: (a) Comparison between LES & RANS models: Liquid penetration length, (b) Comparison between LES & RANS models: Liquid width at $z = 15$ mm axial cross-section from nozzle exit, and (c) Comparison between LES & RANS models: Liquid width at $z = 25$ mm axial cross-section from nozzle exit

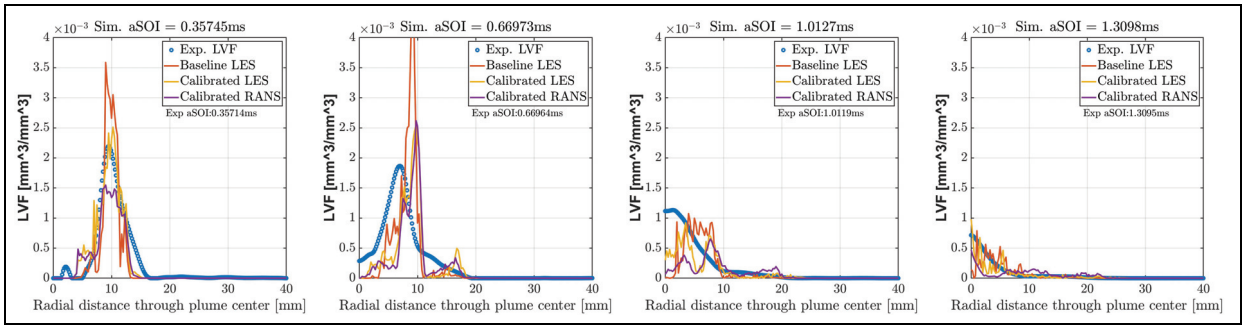

Figure 20. Quantitative plume-averaged liquid volume fraction (LVF) at $z = 15$ mm axial cross-section from nozzle exit: Comparison between LES & RANS models.

more accurately captures the outward sweeping motion of the spray plumes (rotating and expanding motion of the spray tips). These discrepancies likely stem from the predicted droplet diameters at the plume tips, which are possibly larger than those in the experiment.

Conclusions

This study validated CFD models employing the Lagrangian-Eulerian framework for methanol sprays in a constant volume chamber environment. The simulated conditions replicated late-injection DI engine operation using the ECN spray M eight-hole counterbore injector operating at 200 bar injection pressure. For model validation, we utilized the publicly available methanol Spray M1 data according to the new ECN guidelines using the PLV maps generated by the LVF results. The performance of various modeling aspects (i.e. breakup model, turbulence approach, and plume cone angle) was investigated opting to recreate the experimental spray morphology and plume collapsing.

To obtain accurate numerical results, we conducted an extensive sensitivity analysis on the KH-RT breakup model constants using the RANS turbulence approach. By identifying the breakup constants contribution on the models, we calibrated the RANS model and obtained satisfying predictions of the spray morphology, liquid penetration, and liquid plume width. Despite the intensive tuning efforts, the experimentally observed methanol plume collapsing was weakly replicated by the RANS approach. This hindered post-injection methanol spray evolution, resulting in discrepancies in the LVF distribution, and spray collapse behavior. Based on the calibrated RANS model settings, we ran a high-fidelity LES model, which yielded adequate plume collapsing and spray sweeping.

In summary, the present study contributed a methodological investigation of spray modeling, which enabled a calibrated methanol injection model suitable for DI multi-hole injectors under late-injection conditions. Although the RANS model only partially captured the plume collapse and sweeping motions, it provided an adequate prediction of the overall spray morphology, rendering it suitable for engineering-level ICE simulations. Using computationally cheaper RANS models can provide a solid basis for the calibration of more computationally intensive LES simulations. Furthermore, the inherent dissimilarities of the methanol sprays may cause delayed evaporation and increase the chances of wall wetting. This phenomena can potentially increase emissions and hinder engine stability. The proposed modeling approach can aid in optimizing these challenges by implementing

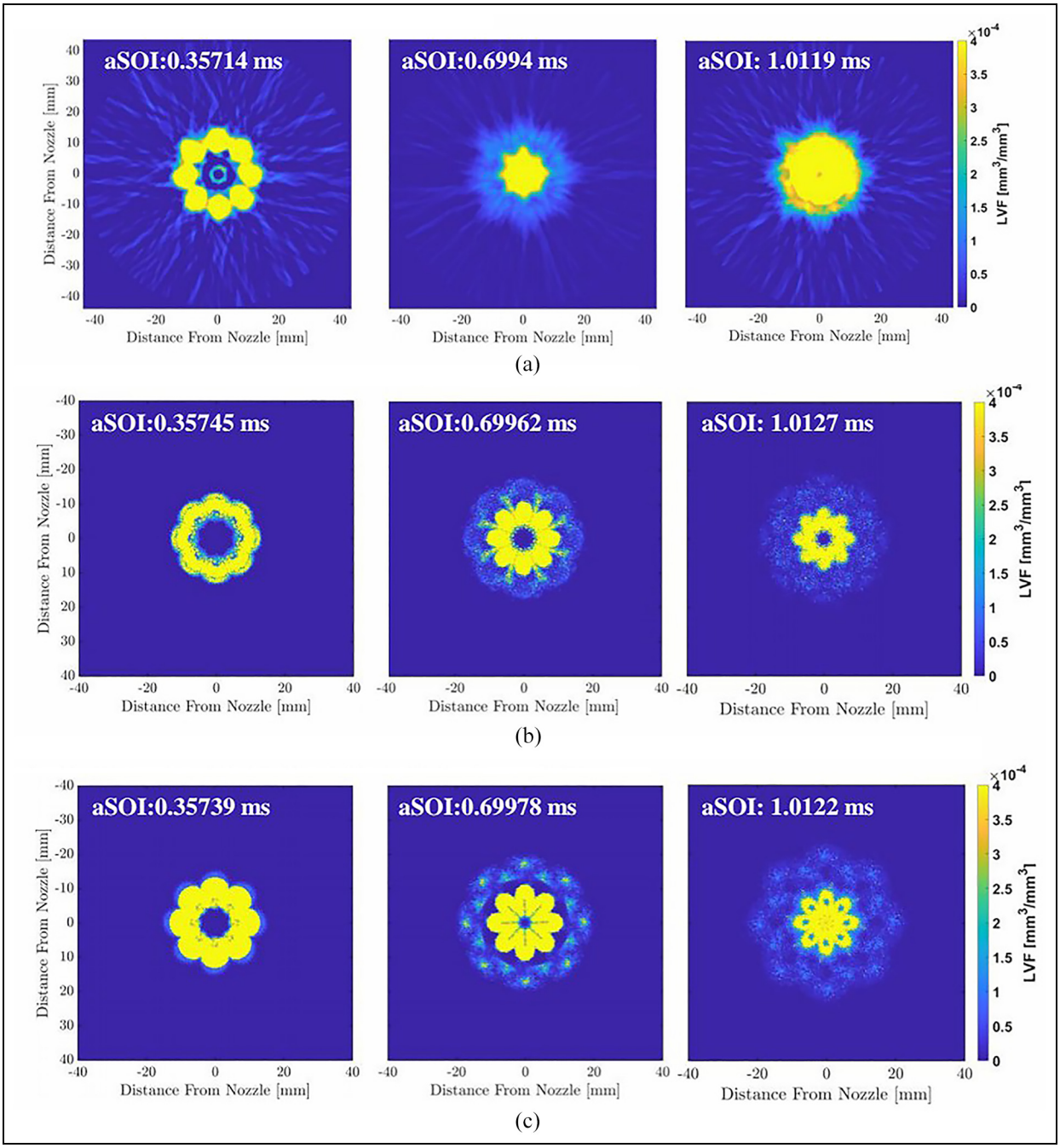

Figure 21. Qualitative XY-plane Liquid Volume Fraction (LVF) distribution at z = 15mm axial cross-section from nozzle exit: Comparison between Experimental LVF (a), Baseline LES Model (b) & Calibrated LES Model (c).

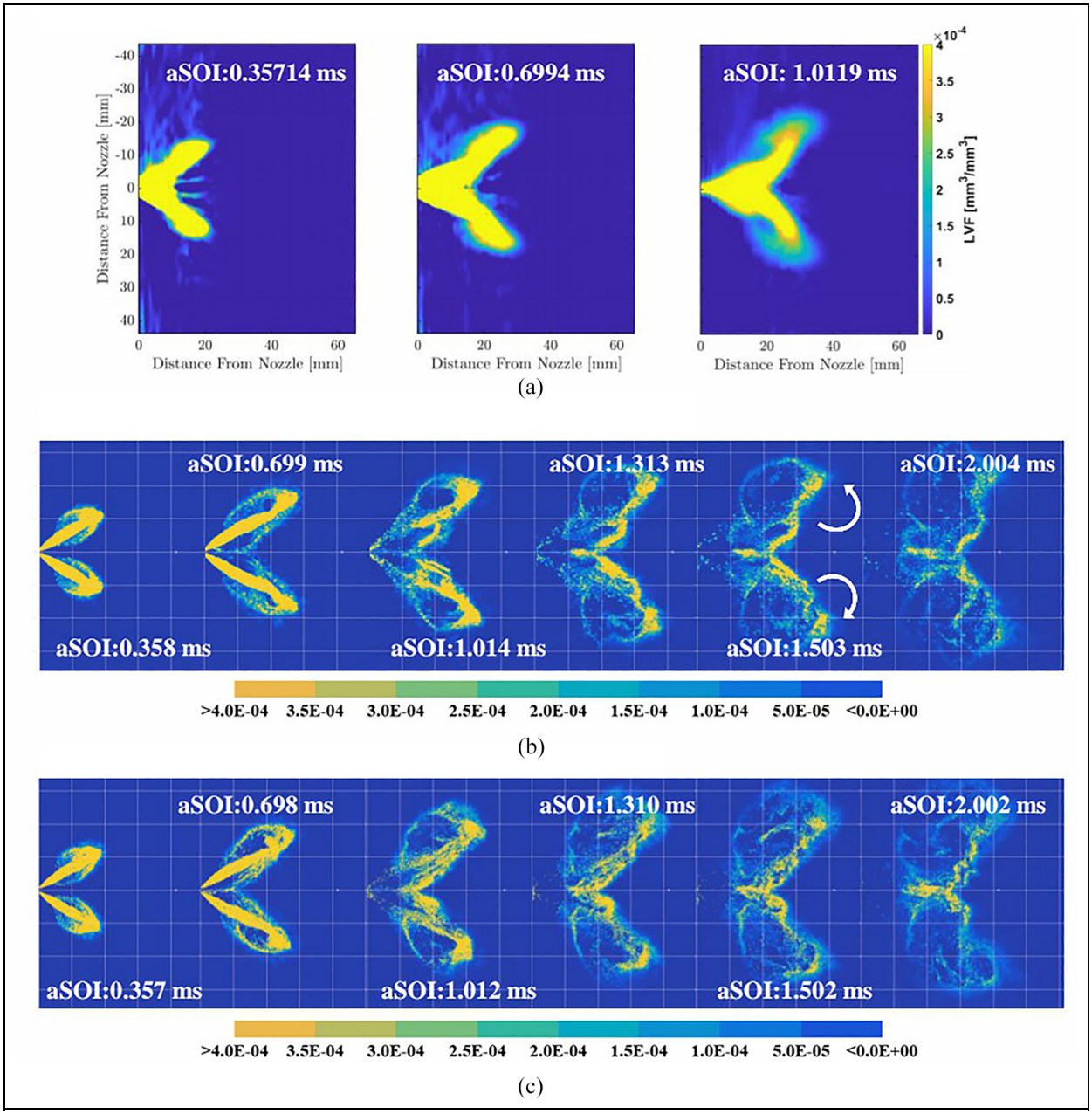

Figure 22. Qualitative YZ-plane liquid volume fraction (LVF): Comparison between Experimental LVF (a), Calibrated RANS Model (b) & Calibrated LES Model (c). In the CFD results each box represents a dimension of 10 mm.

split-injection strategies to minimize spray collapsing, or increasing the intake air temperature to enhance methanol evaporation.

Future studies could employ Volume-of-Fluid (VoF) methods to simulate in-nozzle flow conditions, providing insights into the complex cavitation, evaporation, and turbulence phenomena during methanol injection. Additionally, precise estimation of nozzle coefficients could help reduce discrepancies in the spray momentum predictions. Further experimental work should focus on near-nozzle and droplet size measurements to support the development and calibration of more accurate RANS models. This will enable future CFD models to capture the cavitation-driven effects affecting methanol spray collapse. Our study offers valuable insights into the modeling of methanol spray behavior in DI engines, potentially contributing to the advancement of sustainable methanol-powered engines.

Acknowledgements

We are grateful to the Engine Combustion Network (ECN)[21] for rendering their database publicly available. We would like to thank Convergent Science,[39] and BETA CAE Systems[61] for offering their software (CONVERGE, ANSA & META) and their technical support for the accomplishment of this research. ANSA was used for geometry creation and pre-processing of the CFD model, CONVERGE for the CFD simulations, and META for post-processing and visualization of the results. All simulations were run in parallel using the DelftBlue supercomputer.[62] Lastly, we would also like to thank Dr. Tuan Nguyen for providing the ECN post-processing scripts and Dr. Hao-Pin Lien for the valuable discussions on the Lagrangian modeling of ECN Spray M.

Acronyms

ICE	Internal combustion engine
CFD	Computational fluid dynamics
ECN	Engine combustion network
PFI	Port fuel injection
LPT	Lagrangian particle tracking
RANS	Reynolds averaged Navier Stokes
LES	Large Eddy Simulation DISI Direct-injection spark-ignition
DI	Direct injection
GDI	Gasoline direct-injection
SV	Spray vessel
PISO	Pressure implicit with splitting of operators
CFL	Courant-Friedrichs-Lewy
AMR	Adaptive mesh refinement
TKE	Turbulent kinetic energy
KH-RT	Kelvin Helmholtz - Rayleigh Taylor
TAB	Taylor Analogy Breakup
NTC	No time counter
a SOI	after Start-of-injection
EOI	End-of-injection
VoF	Volume-of-Fluid
LVF	Liquid Volume Fraction
PLV	Projected Liquid Volume

Declaration of conflicting interests

The author(s) declared no potential conflicts of interest with respect to the research, authorship, and/or publication of this article.

Funding

The author(s) disclosed receipt of the following financial support for the research, authorship, and/or publication of this article: The present research is part of the MENENS project (Methanol als Energiestap Naar Emissieloze Nederlandse Scheepvaart). The project is funded by the Netherlands Enterprise Agency (RVO: Rijksdienst voor Ondernemend Nederland) under the grant number MOB21012.

ORCID iD

Konstantinos Zoumpourlos https://orcid.org/0000-0003-1046-5613

References

1. Kessel DG. Global warming—facts, assessment, countermeasures. *J Pet Sci Eng* 2000; 26(1–4): 157–168.
2. Tuner M. Review and benchmarking of alternative fuels in conventional and advanced engine concepts with emphasis on efficiency, CO2, and regulated emissions. *SAE technical papers*, 2016.
3. Duronio F, De Vita A, Montanaro A and Villante C. Gasoline direct injection engines–a review of latest technologies and trends. Part 2. *Fuel* 2020; 265: 116947.
4. Reitz RD, Ogawa H, Payri R, et al. IJER editorial: the future of the internal combustion engine. *Int J Engine Res* 2020; 21(1): 3–10.
5. Kalghatgi G. Is it really the end of internal combustion engines and petroleum in transport? *Appl Energy* 2018; 225: 965–974.
6. Alkidas AC and El Tahry SH. Contributors to the fuel economy advantage of DISI engines over PFI engines. *SAE technical paper*, 2003.
7. Duronio F, De Vita A, Allocca L and Anatone M. Gasoline direct injection engines–a review of latest technologies and trends. Part 1: Spray breakup process. *Fuel* 2020; 265: 116948.
8. Curran S, Onorati A, Payri R, et al. The future of ship engines: renewable fuels and enabling technologies for decarbonization. *Int J Engine Res* 2023; 25(1): 85–110.
9. Zoumpourlos K, Coraddu A, Geertsma R, et al. Evaluation of methanol sprays in marine internal combustion engines: a case study for port fuel injection systems. In: *Modelling and optimisation of ship energy systems* 2023.
10. Agarwal AK, Gautam A, Sharma N, et al. *Methanol and the alternate fuel economy*. Singapore: Springer, 2019.
11. Verhelst S, Turner JW, Sileghem L and Vancoillie J. Methanol as a fuel for internal combustion engines. *Prog Energy Combust Sci* 2019; 70: 43–88.
12. Shamun S, Shen M, Johansson B, et al. Exhaust PM emissions analysis of alcohol fueled heavy-duty engine utilizing PPC. *SAE Int J Engines* 2016; 9(4): 2142–2152.
13. Tripathi A, Park S, Agarwal A, et al. Greener and scalable e-fuels for decarbonization of transport. In: Agarwal AK and Valera H (eds) *Energy, environment, and sustainability*. Singapore: Springer Nature, 2022.
14. Zoumpourlos K, Geertsma R, van de Ketterij R, et al. Methanol operation in heavy-duty DICI dual-fuel engines: investigating charge cooling effects using ECN spray D data. In: *ASME ICEF*, 2024.
15. Wijeyakulasuriya S, Kim J, Probst D, et al. Enabling powertrain technologies for Euro 7/VII vehicles with computational fluid dynamics. *Transp Eng* 2022; 9: 100127.
16. Wang X, Gao J, Jiang D, Huang Z and Chen W. Spray characteristics of high-pressure swirl injector fueled with methanol and ethanol. *Energy Fuels* 2005; 19(6): 2394–2401.
17. Zeng W, Xu M, Zhang M, et al. Characterization of methanol and ethanol sprays from different DI injectors by using MIE-scattering and laser induced fluorescence at potential engine cold-start conditions. *SAE technical papers*, 2010.
18. Zeng W, Xu M, Zhang G, Zhang Y and Cleary DJ. Atomization and vaporization for flash-boiling multi-hole sprays with alcohol fuels. *Fuel* 2012; 95: 287–297.
19. Zeng W, Xu M, Zhang M, Zhang Y and Cleary DJ. Macroscopic characteristics for direct-injection multi-hole sprays using dimensionless analysis. *Exp Therm Fluid Sci* 2012; 40: 81–92.

20. Badawy T, Xu H and Li Y. Macroscopic spray characteristics of iso-octane, ethanol, gasoline and methanol from a multi-hole injector under flash boiling conditions. *Fuel* 2022; 307: 121820.
21. Engine combustion network. 2023. https://ecn.sandia.gov/ (accessed 1 September 2023).
22. Engine combustion network Spray-G conditions. 2023. https://ecn.sandia.gov/gasoline-spray-combustion/target-condition/spray-g-operating-condition/ (accessed 5 February 2024).
23. Engine combustion network Spray-M data. 2023. https://ecn.sandia.gov/data/sandia-spray-m-data/ (accessed 5 February 2023).
24. Hwang J, Weiss L, Karathanassis IK, Koukouvinis P, Pickett LM and Skeen SA. Spatio-temporal identification of plume dynamics by 3D computed tomography using engine combustion network Spray G injector and various fuels. *Fuel* 2020; 280: 118359.
25. Svensson M, Tuner M and Verhelst S. Low load ignitability of methanol in a heavy-duty compression ignition engine, pp. 2022–NaN01–1093.
26. Zincir B, Shukla P, Shamun S, Tuner M, Deniz C and Johansson B. Investigation of effects of intake temperature on low load limitations of methanol partially premixed combustion. *Energy Fuels* 2019; 33(6): 5695–5709.
27. Dong Y, Kaario O, Hassan G, Ranta O, Larmi M and Johansson B. High-pressure direct injection of methanol and pilot diesel: a non-premixed dual-fuel engine concept. *Fuel* 2020; 277: 117932.
28. Matamis A, Lonn S, Luise L, et al. Optical characterization of methanol compression-ignition combustion in a heavy-duty engine. In: *Proceedings of the combustion institute*, vol. 38, pp.5509–5517. Elsevier Ltd.
29. Wouters C, Burkardt P, Steeger F, Fleischmann M and Pischinger S. Comprehensive assessment of methanol as an alternative fuel for spark-ignition engines. *Fuel* 2023; 340: 127627.
30. Dierickx J, Verbiest J, Janvier T, Peeters J, Sileghem L and Verhelst S. Retrofitting a high-speed marine engine to dual-fuel methanol-diesel operation: a comparison of multiple and single point methanol port injection. *Fuel Commun* 2021; 7: 10.
31. Konstantinos KI, de Vos P, Zoumpourlos K, et al. Methanol for heavy-duty internal combustion engines: review of experimental studies and combustion strategies. *Renewable and Sustainable Energy Reviews* 2025; 214: 115529.
32. Duronio F, Lien HP and De Vita A. CFD unified approach under Eulerian–Lagrangian framework for methanol and gasoline direct injection sprays in evaporative and flash boiling conditions. *Int J Multiphase Flow* 2025; 182: 105048.
33. Paredi D, Lucchini T, D'Errico G, Onorati A, Pickett L and Lacey J. Validation of a comprehensive computational fluid dynamics methodology to predict the direct injection process of gasoline sprays using spray g experimental data. *Int J Engine Res* 2020; 21(1): 199–216.
34. Kumar A and Van Dam N. Study of injector geometry and parcel injection location on spray simulation of the engine combustion network Spray G injector. *J Eng Gas Turbine Power* 2023; 145(7): 071012.
35. Kumar A, Boussom JA and Van Dam N. Large-eddy simulation study of injector geometry and parcel injection location on spray simulation of the engine combustion network Spray G injector. *J Eng Gas Turbine Power* 2024; 146(8): 081003.
36. Lien HP, Li Y, Pati A, Sadiki A and Hasse C. Numerical studies of gasoline direct-injection sprays (ECN spray G) under early-and late-injection conditions using large eddy simulation and droplets-statistics-based Eulerian–Lagrangian framework. *Fuel* 2024; 357: 129708.
37. Bestel D, Kim J, Zhao L, et al. A comprehensive numerical investigation on spray models for direct-injection spark-ignition engines. *Fuel* 2024; 373: 132325.
38. Moreno Cabezas K, Liu X and Im H. Characteristics of methanol and iso-octane under flashing and non-flashing conditions in ECN-G spray, 2022.
39. CONVERGE CFD software website. 2023. https://convergecfd.com/ (accessed 13 November 2023).
40. Liquid penetration length. 2024. https://ecn.sandia.gov/diesel-spray-combustion/experimental-diagnostics/liquid-penetration-length/ (accessed 16 February 2023).
41. Lien HP and Mallad RC. Intake-injection Spray G and Spray M research using methanol and PACE-20 simulation. In: *ECN9 proceedings presentation*. Engine Combustion Network. https://ecn.sandia.gov/workshop/ECN9/ECN9_Spray_GM.pptx (accessed 20 March 2023).
42. Weiss L, Wensing M, Hwang J, Pickett LM and Skeen SA. Development of limited-view tomography for measurement of Spray G plume direction and liquid volume fraction. *Exp Fluids* 2020; 61(2): 1–17.
43. Subramaniam S. Lagrangian–Eulerian methods for multiphase flows. *Prog Energy Combust Sci* 2013; 39(2-3): 215–245.
44. Han Z and Reitz RD. Turbulence modeling of internal combustion engines using RNG - models. *Combust Sci Technol* 1995; 106(4-6): 267–295.
45. Pomraning E and Rutland CJ. Dynamic one-equation nonviscosity large-eddy simulation model. *AIAA J* 2002; 40(4): 689–701.
46. Convergent science Inc. Converge manual v3.0, (2022, accessed 5 July 2022).
47. Issa RI. Solution of the implicitly discretised fluid flow equations by operator-splitting. *J Comput Phys* 1986; 62(1): 40–65.
48. Ferziger JH, Perić M and Street RL. *Computational methods for fluid dynamics*. Berlin, Heidelberg: Springer, 2002. Vol. 3.
49. Horvath AL. Redlich-kwong equation of state: review for chemical engineering calculations. *Chem Eng Sci* 1974; 29(5): 1334–1340.
50. Reitz RD and Diwakar R. Structure of high-pressure fuel sprays. *SAE transactions* 1987, pp.492–509.
51. Reitz RD and Beale JC. Modeling spray atomization with the Kelvin-Helmholtz/Rayleigh-Taylor hybrid model. *Atomization Sprays* 1999; 9(6): 623–650.
52. Schmidt DP and Rutland CJ. A new droplet collision algorithm. *J Comput Phys* 2000; 164(1): 62–80.

53. Post SL and Abraham J. Modeling the outcome of drop–drop collisions in diesel sprays. *Int J Multiphase Flow* 2002; 28(6): 997–1019.
54. Liu AB, Mather D and Reitz RD. Modeling the effects of drop drag and breakup on fuel sprays. *SAE transactions* 1993, pp.83–95.
55. O'Rourke PJ. Statistical properties and numerical implementation of a model for droplet dispersion in a turbulent gas. *J Comput Phys* 1989; 83(2): 345–360.
56. Patterson MA and Reitz RD. Modeling the effects of fuel spray characteristics on diesel engine combustion and emission. *SAE transactions* 1998, pp.27–43.
57. Di Matteo A, Bao H and Somers B. Modeling Spray C and Spray D with FGM within the framework of RANS and LES. *Front Mech Eng* 2022; 8: 1013138.
58. Senecal P, Pomraning E, Richards K, et al. Grid-convergent spray models for internal combustion engine CFD simulations. In: *Internal combustion engine division fall technical conference*, vol. 55096, pp.697–710. American Society of Mechanical Engineers.
59. Mohan B, Badra J, Sim J and Im HG. Coupled in-nozzle flow and spray simulation of engine combustion network Spray-G injector. *Int J Engine Res* 2021; 22(9): 2982–2996.
60. Duronio F, Ranieri S, Montanaro A, Allocca L and De Vita A. ECN Spray G injector: numerical modelling of flash-boiling breakup and spray collapse. *Int J Multiphase Flow* 2021; 145: 103817.
61. BETA CAE systems website, 2023. https://www.beta-cae.com/ (accessed 13 November 2023).
62. Delft high performance computing centre (DHPC). Delftblue supercomputer (Phase 1), 2022. https://www.tu9delft.nl/dhpc/ark/delftbluephase1 (accessed 13 November 2023).

Appendix

Effect of plume cone angle on spray collapsing

In this subsection, we consider the influence of cone angle on spray characteristics as an additional calibration parameter. The cone angle strongly influences liquid penetration and spray jet morphology, and hence, appropriate tuning is compulsory. An increased cone angle negatively affects spray momentum due to higher air entrainment rate, enabling elevated mixing and evaporation. In addition, elevated cone angle values create a less dense spray liquid core and promote inter-plume interactions. To successfully recreate the experimental injection phenomena, increasing the inter-plume interactions can enhance spray collapsing and subsequently, spray sweeping phenomena.

In the RANS model, the effect of the cone angle was less intensive than expected and slightly affected spray plume collapsing. For both the RANS and LES cases, a cone angle value of 33° was selected as the most appropriate for obtaining an adequate prediction of the liquid length (Figure 23 and Figure 24). However, in the RANS case, the selected cone angle did not represent well the spray liquid width due to the model's weakness in fully capturing spray collapsing and sweeping phenomena. Figure 25 presents the RANS model insensitivity to cone angle perturbations using the LVF in the radial direction of the 15 mm downstream cross-section.

On the contrary, the LVF of the LES model presents greater sensitivity to the cone angle (Figure 26). Overall, the LES model performed better than RANS, and achieved better predictions of the experiment by accurately recreating the desired spray momentum and morphology. Interestingly, for the early stages of the spray formation prior to EOI, the smaller cone angles exhibited the expected increased liquid penetration. After the EOI, especially the 35° cone angle model displays a more intense collapsing as highlighted by the elevated LVF values near the nozzle center-line at 0.67 ms. This spray collapsing phenomenon generates an excessive accumulation of liquid droplets in the center-line of the spray. Consequently, this bulk of liquid fuel merges and forms a single high-momentum plume, which eventually, increases liquid penetration.

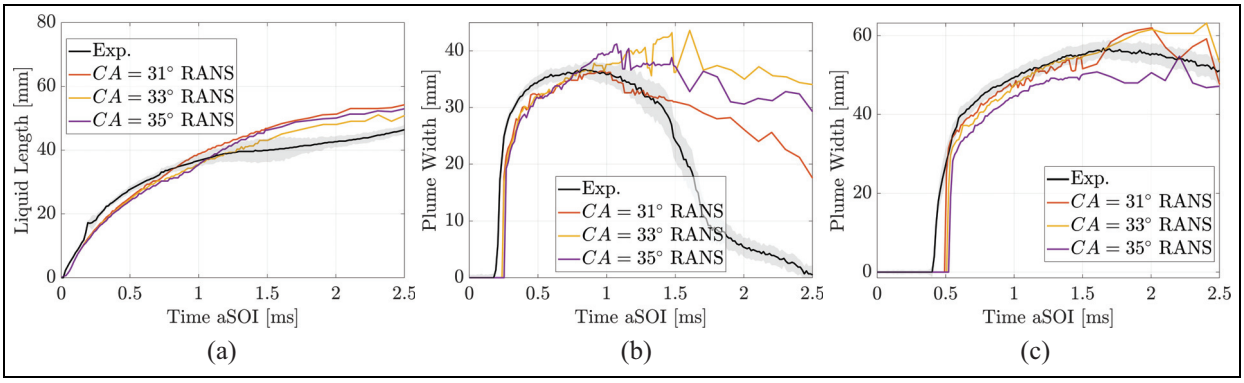

Figure 23. RANS model cone angle influence: Liquid penetration & width: (a) RANS model cone angle influence: Liquid penetration length, (b) RANS model cone angle influence: Liquid width at $z = 15$ mm axial cross-section from nozzle exit, and (c) RANS model cone angle influence: Liquid width at $z = 25$ mm axial cross-section from nozzle exit.

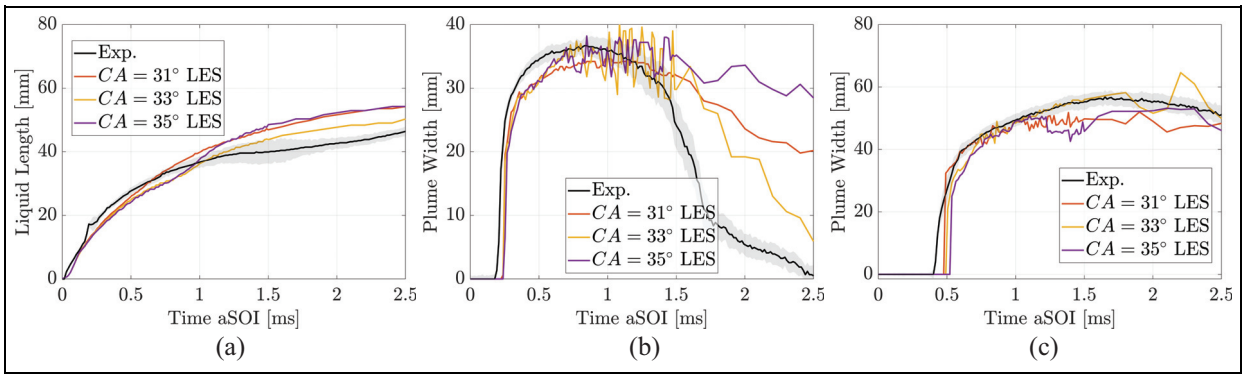

Figure 24. LES model cone angle influence: Liquid penetration & width: (a) LES model cone angle influence: Liquid penetration length, (b) LES model cone angle influence: Liquid width at $z = 15$ mm axial cross-section from nozzle exit, and (c) LES model cone angle influence: Liquid width at $z = 25$ mm axial cross-section from nozzle exit.

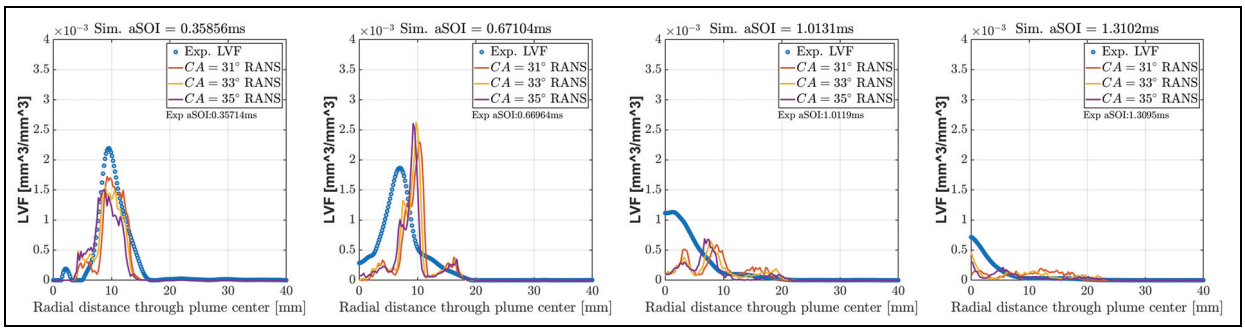

Figure 25. Quantitative plume-averaged liquid volume fraction (LVF) at $z = 15$ mm axial cross-section from nozzle exit: Impact of cone angle in RANS Model.

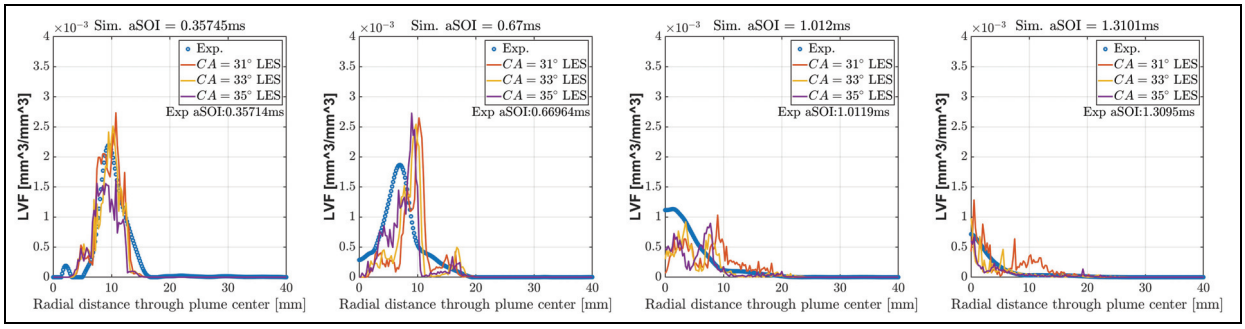

Figure 26. Quantitative plume-averaged liquid volume fraction (LVF) at $z = 15$ mm axial cross-section from nozzle exit: Impact of cone angle in LES model.